GROWTH AND STRUCTURAL CHARACTERIZATION OF Fe/TaO_x/Fe MAGNETIC MULTILAYERS

A Thesis Submitted to
the Graduate School of Engineering and Sciences of
İzmir Institute of Technology
in Partial Fulfillment of the Requirements for the Degree of

MASTER OF SCIENCE

in Physics

by
Kaan OĞUZ

June 2006
İZMİR

We approve the thesis of **Kaan OĞUZ**

Date of Signature

..... **29 June 2006**
Assist. Prof. Süleyman TARI
Supervisor
Department of Physics
İzmir Institute of Technology

..... **29 June 2006**
Assoc. Prof. Mürsel ALPER
Department of Physics
Uludağ University

..... **29 June 2006**
Prof. Dr. Doğan ABUKAY
Department of Physics
İzmir Institute of Technology

..... **29 June 2006**
Prof. Dr. Durmuş ALİ DEMİR
Head of the Department
İzmir Institute of Technology

.....
Assoc. Prof. Semahat ÖZDEMİR
Head of the Graduate School

ACKNOWLEDGEMENTS

First, I would like to thank my thesis advisor Assist. Prof. Süleyman TARI for his motivative talks, academic guidance, beneficial discussions, and continuous support throughout all phases of this thesis. I want to express my great thankfulness to Assoc. Prof. Lütfi ÖZYÜZER for his valuable suggestions and help both in laboratory and in my thesis.

I especially want to express my gratitude to my wife Deniz and my family for their motivation and great support during my master study in Izmir Institute of Technology.

I would like to thank to the staff of the Center for Material Research of Izmir Institute of Technology for their help and great contribution to this study. I acknowledge to Izmir Institute of Technology for providing Research Assistantship and project funding (IYTE-BAP 34 2005) during my thesis.

I want to thank my lab-mates Savaş Ulucan, Kadir Vahaplar, Yılmaz Şimşek, and Mehtap Özdemir for their support, creation of a friendly atmosphere in the lab and valuable scientific discussions.

ABSTRACT

GROWTH AND STRUCTURAL CHARACTERIZATION OF $Fe/TaO_x/Fe$ MAGNETIC MULTILAYERS

In this thesis, we are proposing to fabricate and structurally characterize $Fe/TaO_x/Fe$ magnetic multilayers as an initiative work towards magnetic tunnel junction (MTJ) structures with TaO_x spacer layer. The multilayer structures were grown by magnetron sputtering technique and characterized by X-Ray Diffraction (XRD), Atomic Force Microscopy (AFM), and Scanning Electron Microscopy (SEM). Ellipsometry was used to find the refractive index and the hysteresis loops were taken by SQUID Magnetometer. It was found that Fe grew 45 degree tilted epitaxial single crystal on Si (001) substrate at room temperature. Ta growth on silicon had poor crystal quality due to large lattice mismatch between tantalum and silicon however Ta single layer on Fe was found to be single crystal with 0.72 FWHM. Reactive oxidation of Ta film resulted in formation of amorphous Ta_2O_5 with refractive index of 2.1. Fe, Ta, and TaO_x single layer films were found to be uniform and smooth on silicon substrate. Bilayer of Fe/Ta and Fe/TaO_x were also investigated to understand the behavior of single layer films on top of each other. Multilayers with Ta and TaO_x spacer layers were successfully grown and these multilayers showed good structural properties. Furthermore, hysteresis loops of Fe films as thin as 50 nm showed magnetization comparable with the bulk Fe with the coercive field of 20 Oe.

ÖZET

$Fe/TaO_x/Fe$ MANYETİK ÇOKLU KATMANLARIN BÜYÜTÜLMESİ VE YAPISAL ÖZELLİKLERİNİN İNCELENMESİ

Bu tezde, $Fe/TaO_x/Fe$ manyetik çoklu katmanların büyütülmesi ve yapısal özelliklerinin incelenmesi önerilmektedir. Bu çalışma TaO tabanlı manyetik tünel eklemi (MTJ) üretimi projesinin başlangıç safhası olacaktır. Çoklu katmanların üretimi mıknatıssal sıçratma tekniği ile gerçekleştirilmiş ve yapısal incelemesi XRD, SEM ve AFM teknikleri kullanılarak yapılmıştır. Elipsometri tekniği kırılma indisi bulmakta ve SQUID manyetometrisi ise histeresis eğrilerini incelemekte kullanılmıştır. Demir ince filimin, Si (001) alttaş üzerine 45 derece dönük epitaksiyel tek kristal olarak büyüdüğü görülmüştür. Bunun yanı sıra tantalum filimi demirin aksine silikon üzerine çok düşük kalitede büyümüştür. Bunun ana sebebi Ta ile Si arasındaki büyük örgü parametresi uyuşmazlığıdır. Fakat tantalum, demir ince filim üzerine tek kristal olarak büyümüştür. Ta metalini reaktif oksitleme tekniği ile 2.1 kırılma indisine sahip amorf Ta_2O_5 elde edilmiştir. Fe, Ta ve TaO_x ince filimlerinin silikon alttaş üzerine oldukça homojen ve pürüzsüz olarak kaplandığı anlaşılmıştır. Tek katmanlı filimlere ek olarak Fe/Ta ve Fe/TaO_x çift katmanlı yapıları büyütülüp filimlerin birbirleri üzerine nasıl büyüdükleri incelenmiştir. Ta ve TaO_x arayüzeyli çok katmanlı yapılar başarılı bir şekilde büyütülmüş ve bunların iyi yapısal özellikler gösterdiği bulunmuştur. Ayrıca, 50 nm kalınlıktaki demir ince filimin histeresis eğrisi bu filimin tamamen ferromanyetik olduğunu göstermiştir.

TABLE OF CONTENTS

LIST OF FIGURES

LIST OF TABLES

CHAPTER 1

INTRODUCTION

The motivation in electronics technology is towards producing faster and smaller devices. Therefore, the research community is working on new types of materials and fabrication methods to achieve these requirements. However, there are some problems for today's electronics technology. The miniaturization and the non-volatility can be counted as main problems. To overcome these problems, scientists are nowadays trying to adopt quantum mechanical phenomena in computer and electronics technology. Spin of the electron is purely quantum mechanical phenomena and has become a major issue of research in quantum electronic device technology, recently.

Spintronics -acronym for spin-electronics or magnetoelectronics- is a new research field in condensed matter physics which is based on the control of the spin or spin + charge property of the electron. In conventional electronic devices, spin property of the electron has been ignored until recently. One of the major reasons for this was the lack of proper film growth techniques to integrate magnetic materials with nonmagnetic ones, especially with semiconductors. With the advances in growth techniques such as molecular beam epitaxy and magnetron sputtering, it has been possible to integrate the magnetic materials with the present electronics technology. Spintronic devices have already started replacing conventional electronic devices. For example the first spintronic device, GMR read head, have been used in computer hard disks since 1994 (Tsang et al. 1994). These devices have advantages over conventional electronic devices such as non-volatility, low-power consumption, high speed, and operation at very small scales (nano-meters). Examples for spintronics devices are magnetic sensors, magnetic memory, spin transistors, spin LED etc.

Data storage industry mainly relies on the storage of data on magnetic media such as hard disk drives. Magnetic sensors are used in hard disks as read heads. The inductive coils were used to read and write the information on magnetic recording media but its operation principle and structural design did create certain limitations to its performance. Important studies on magnetic field sensors started with *Anisotropic Magnetoresistance* (AMR) effect. It was used in early hard disc read heads. In early 1990s, AMR based read heads were put into market by IBM. The AMR effect is the

result of the spin-orbit interaction of electrons within the ferromagnetic materials (Wang and Taratorin 1999). The spin-orbit interaction is the interaction between the spin and the angular momentum of the electron under external magnetic field. Resistance of the ferromagnetic material changes depending on the relative orientation of the magnetization and the direction of the current as shown in Fig. 1.1. Ferromagnetic material shows high resistance when the magnetization and the current direction are parallel whereas, the resistance of the material is small when they are perpendicular (Fig. 1.1). The angle dependent resistivity is calculated by

$$\rho(\varphi) = \rho_{\perp} + (\rho_{//} - \rho_{\perp}) \cdot \cos^2 \varphi \tag{1.1}$$

where $\rho_{//}$ and $\rho_{\perp}$ are the resistivities of parallel and perpendicular alignment of the current direction and the magnetization, respectively and φ is the angle between magnetization and the current direction. In addition, the change in the resistance (AMR ratio) is found by;

$$MR = \frac{\rho_{//} - \rho_{\perp}}{\rho_{//}} \tag{1.2}$$

However, the change in the resistance due to AMR was quite small, in the order of 2-5 percents. Permalloys ($Ni_{70}Co_{30}$, etc.) were the common materials that were used in AMR read heads (McGuire and Potter 1975). On the other hand; MR ratio decreases linearly with thickness for thin films (<10 nm).

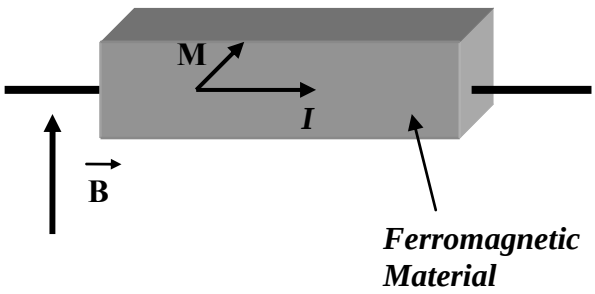

Figure 1.1. Schematic of AMR effect observed in some ferromagnetic materials.

The discovery of *Giant Magnetoresistance* (GMR) effect in 1988 by Baibich et al. (Baibich et al. 1988) attracted a great attention. This effect was first discovered in Fe/Cr multilayers. GMR effect is observed in heterostructures that are composed of two ferromagnetic metals (FM) separated by a nonmagnetic metal (NM) spacer layer, as shown in Fig. 1.2.

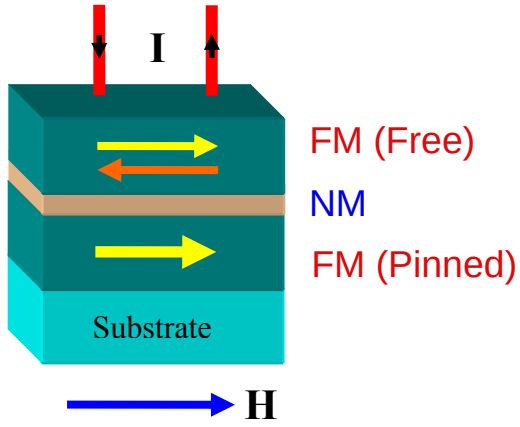

Figure 1.2. Schematic of FM/NM/FM structure (spin valve).

The simple three layer structure consisting of FM/NM/FM structure is called spin-valve. The horizontal arrows in the figure represent the magnetization directions of the ferromagnetic layers. In the absence of magnetic field the FM layers are anti-ferromagnetically coupled resulting in high resistance. FM layers couple ferromagnetically under external magnetic field (H) resulting in a decrease in the resistance of the structure.

In Fig. 1.3, the normalized resistance vs. magnetic field response of Fe/Cr layers is illustrated. The big change in the resistance can easily be observed in the graph. Increase in Cr layer thickness results in a decrease in the resistance ratio; this is due to the spin-flip scattering of electrons within the conductor. Important thing to be noticed in this study is that FM layers are coupled anti-ferromagnetically or ferromagnetically depending on the non-magnetic metal layer thickness when the external magnetic field (H) is zero. This effect is called oscillatory spin coupling.

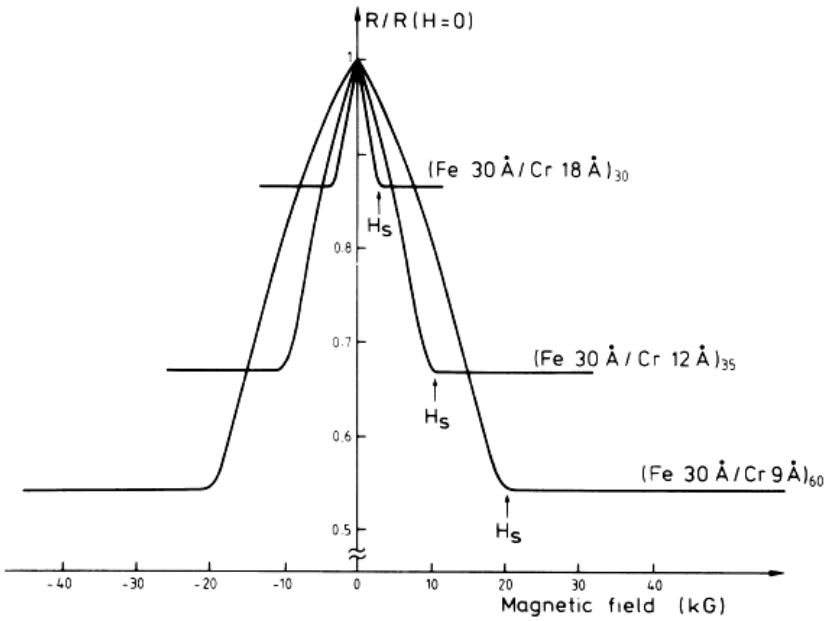

Figure 1.3. R/R(H=0) vs. magnetic field graph of Fe/Cr multilayers (Source: Baibich et al. 1988).

Ferromagnetic layers should have different saturation fields in spin valve structures. Otherwise, the applied field H may change the magnetizations of both FM layers. Therefore, one of the FM layers should be pinned. This is achieved either by using ferromagnetic materials which have different coercive fields or using an exchange bias layer which is an antiferromagnet. This effect is named giant because the relative change in the resistance is very high compared to AMR effect (2-5 %). GMR ratios up to 85 % at 4.2 K and 19 % at room temperature have been reported by Baibich et. al.

The origin of GMR effect is quite different from conventional resistance. Generally, the bulk resistance is caused by scattering of electrons by crystal defects, phonons, and other electrons etc. This is calculated roughly by,

$$R = \frac{\rho L}{A} \tag{1.3}$$

However, GMR effect is based on the spin dependent scattering of the electrons. Spin polarized electrons are scattered at the interfaces depending on the orientation of the magnetization of the second electrode. This is observed for structures with the size in

the order of mean free path of electrons. Mean free path is the distance traveled by an electron between two successive collisions.

Intensive research on GMR effect resulted in a commercial device application as GMR read head in 1994 (Tsang et al. 1994). Magnetic sensors and the magnetic random access memories are the other device applications of GMR. On the other hand, studies on GMR devices also increased the attention on magnetic thin films and magnetic multilayers.

Tunneling magnetoresistance (TMR) effect is one of the other important and widely studied spintronic effects. This effect is observed in multilayers composed of two ferromagnetic metals separated by an insulator spacer layer. This structure is called magnetic tunnel junction (MTJ) and it is illustrated in Fig. 1.4. In this structure, layer thicknesses are in the order of a few nanometers. The working principle is similar to GMR devices. The relative orientations of the magnetizations of FM electrodes alter the resistance of the structure.

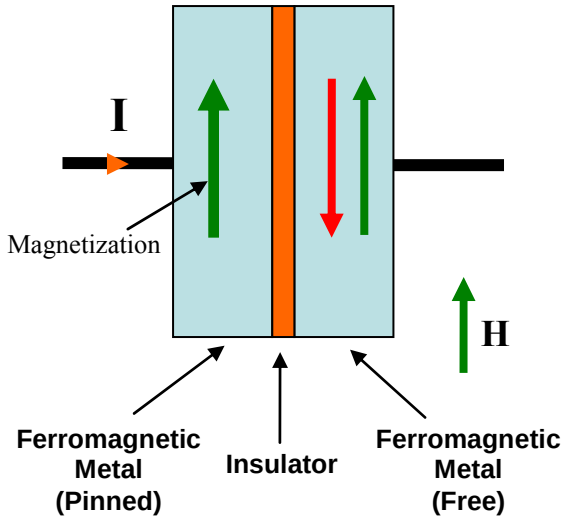

Figure 1.4. Schematic of magnetic tunnel junction composed of FM/I/FM.

The change in the resistance is called tunnel magnetoresistance ratio and calculated by the formula;

$$TMR \equiv \left(\frac{R_{ap} - R_p}{R_p} \right) \times 100 \qquad (1.4)$$

In this expression, R_{ap} and R_p represent the anti-parallel alignment resistance and parallel alignment resistance values of the multilayer, respectively.

In MTJs the transport of electrons is via tunneling phenomenon which is a purely quantum mechanical effect. Basics of this phenomenon will be given here briefly but it has been discussed thoroughly in (Duke 1969 and Wolf 1985). Fig. 1.5, (a) shows decay of the electron's wave-function while tunneling through a potential barrier. Actually, most of the wave is reflected back from the barrier because electrons do not have enough energy to pass over the potential barrier. But the probability of the electrons tunneling through the potential barrier is not *zero*.

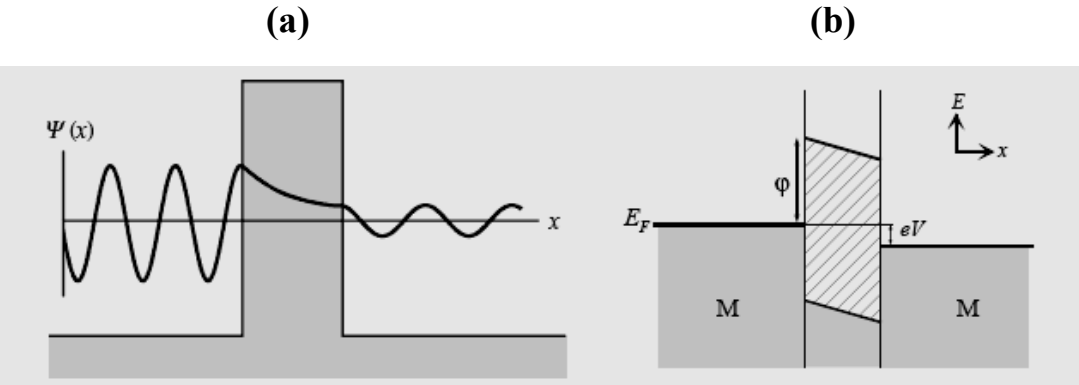

Figure 1.5. (a) Decay of wave-function within the tunneling barrier and (b) band diagram of metal/insulator/metal structure.

Tunneling current in metal/insulator/metal structures (energy band diagram is shown in Fig. 1.5 (b)) is given by

$$I_{l\to r}(V) = \int_{-\infty}^{+\infty} \rho_l(E)\cdot\rho_r(E+eV)\cdot|M|^2\cdot f(E)\cdot[1-f(E+eV)]dE \quad (1.5)$$

This expression describes the tunneling current from left electrode to right electrode. In the equation, $\rho_l(E)$ represents the density of states at a given energy in the left electrode and $\rho_r(E+eV)$ is the density of states at the same energy in the right electrode. $|M|^2$ is the square of the matrix element which is the tunneling probability. $f(E)$ is the probability that the states in the left electrode are occupied and

$[1-f(E+eV)]$ is the probability that the states in the right electrode are empty where $f(E)$ is the Fermi-Dirac distribution function. The total current is given by $I_{l\to r} - I_{r\to l}$. In addition to this basic formula, Simmons (Simmons 1963) proposed a generalized formula for the electrical tunneling between similar electrodes separated by a thin insulating film by solving the current equation. He used WKB approximation to obtain the matrix element $|M|^2$ for an arbitrary barrier of average height above the common Fermi level. His well-known result for a trapezoidal barrier is

$$J(V) = \frac{J_0}{d^2}\left(\overline{\varphi} - \frac{eV}{2}\right)\exp\left[-Ad\sqrt{\overline{\varphi} - \frac{eV}{2}}\right] - \frac{J_0}{d^2}\left(\overline{\varphi} + \frac{eV}{2}\right)\exp\left[-Ad\sqrt{\overline{\varphi} + \frac{eV}{2}}\right] \qquad (1.6)$$

where $J(V)$ is the tunnel current density, $A = 4\pi\sqrt{2m_e^*}/h$ and $J_0 = e/2\pi h$ are constants, m_e^* is the effective mass of the electron, d is the barrier thickness, $\overline{\varphi}$ is the average barrier height above the Fermi level, and eV is the applied bias to the structure. Equation 1.6 has been used (Brinkman et al. 1970) to fit experimental $J(V)$ data to determine effective barrier height and barrier thickness. Exponential dependence on the barrier thickness and the square root of barrier height can easily be observed from this equation. One important thing to mention about this equation is that the electrodes are assumed to be identical.

The early experiments on spin dependent tunneling yielded a change of nearly 14% at 4.2K in the tunnel conductance at zero bias in Co/Ge/Fe junctions (Julliere, 1975). Later studies using barriers like NiO and Al_2O_3 demonstrated definite results for FM/I/FM tunneling (Maekawa and Gäfvert 1982, Miyazaki et al. 1991, Nowak and Rauluszkiewicz 1992, and Le Clair et al., 1994). However, in these experiments, the change in the tunnel resistance was not very significant. Actually, it was not more than one percent at room temperature. In 1995, *Moodera et al.* and *Miyazaki and Tezuka* both discovered high TMR at room temperature. Moodera's group used $CoFe/Al_2O_3/Co$ junctions in their experiment and they achieved change in the resistance up to 11% (Moodera et al. 1995). Miyazaki and Tezuka investigated $Fe/Al_2O_3/Fe$ structure and they found almost 20 % TMR at room temperature (Miyazaki and Tezuka 1995). The discovery of large TMR at room temperature accelerated the study of spin-dependent transport in magnetic thin films.

After these big achievements, different types of barrier and electrode materials have been used in MTJs. Amorphous Al_2O_3 have been the most successful and the most widely used barrier material in literature (Mitsuzuka et al. 1999, Moodera et al. 1995, and Wang et al. 2004). Experiments using oxides like *MgO* (Bowen et al. 2001, Costa-Krämer et al. 2002, Keavney et al. 1997, Mitani et al. 2003, and Przybylski et al. 2002), Ga_2O_3 (Li et al. 2000), HfO_2 (Park et al. 2003), ZrO_x (Wang et al. 2001), YO_x (Dimopoulos et al. 2003), InO_x (Androulakis et al. 2005) and TaO_x (Dorneles et al. 2002, Gillies et al. 2001, Koller et al. 2005, Ladak and Hicken 2005, Platt et al. 1997, and Rottlander et al. 2001) and other barriers like *AlN* (Shim et al. 2002 and Sharma et al. 2004), *ZnS* (Dinia et al. 2003), *EuS* (Smits et al. 2004), *ZnSe* (Gustavsson et al. 2001), *AlAs* (Samarth et al. 2003) and etc. have been also carried out. *Fe*, *Co*, *CoFe*, *NiFe*, and *Permalloys* etc. have been used extensively as ferromagnetic electrodes in magnetic tunnel junctions by different groups. On the other hand, half metallic ferromagnets such as $La_{0.7}Sr_{0.3}MnO_3$ (Barthelemy et al. 2002) and Fe_3O_4 (Takahashi et al. 2004) and ferromagnetic semiconductors like *GaMnAs* (Samarth et al. 2003) are the other material types used in MTJ research.

The fabrication process of MTJ structures is not very straightforward. Since the thicknesses of the films in these structures are about a few nanometers, their deposition process requires extreme care. Especially, growing ultra thin, pinhole-free tunnel barrier is extremely difficult. To have epitaxial or good quality junctions is also hard to achieve. First of all, the bottom electrode should be very flat that is the surface roughness should be 1-3 nm. In this case, the substrate choice is very important. If the lattice mismatch between substrate and the first FM layer is not small enough, first electrode will not be in good quality in terms of crystallinity. Then on top of it, ultra thin barrier should be deposited with very high uniformity. Since quantum mechanical tunneling is required the barrier thickness should not exceed ~100 Å (10 nm). This barrier layer should also be extremely flat to have good quality top electrode. Crystallinity of the electrodes is important in terms of magnetic property.

The interfaces between the barrier and the electrodes are critically important for the magnetic tunnel junctions. Magnetically dead layers should not be present at the interfaces. If so, these dead layers will reduce the device performance by decreasing the TMR value. Spin-polarized electrons should not loose their spin information while passing through interfaces. Therefore, choosing appropriate electrode and barrier is the key issue for MTJ fabrication.

In this thesis, single layer of Fe, Ta and TaO_x as well as $Fe/TaO_x/Fe$ three layer structures were grown by magnetron sputtering system and the structural characterization of the films were investigated. Due to the insufficiencies of the growth and characterization systems, we are unable to grow very thin, ~ 3 nm, films to build magnetic tunnel junctions. Therefore relatively thick ~50 nm of layers were grown and the structural characterization was studied from film growth point of view. This project is a first study towards building MTJ structures.

The rest of the thesis is organized as follows. Chapter 2 will describe the thin film growth kinetics and the basics of sputtering technique. Properties of the materials used in this study are also given in this chapter. Experimental facilities and growth process are explained in Chapter 3. Main focus of Chapter 4 is the interpretation of the results and comparison of these data with literature. Finally, the summary is given in Chapter 5.

CHAPTER 2

THIN FILM GROWTH and MATERIAL PROPERTIES

The purpose of this study is to grow and characterize thin Ferromagnetic (FM)/ Insulator (I)/Ferromagnetic (FM) trilayer structures, namely Fe/TaO_x/Fe. The structural properties of this FM/I/FM layers will be studied.

All layers were grown by magnetron sputtering method. Therefore, it is appropriate to review the basics of thin film growth and the mechanism of the magnetron sputtering technique at this point. Also material properties of Fe, Ta, TaO, and Si will be given in this chapter.

2.1. Growth Kinetics

A thin film is formed through chemical bonding between the atoms/molecules of depositing materials onto a substrate surface. The quality of the films is determined by deposition conditions; mainly by growth temperature, growth rate, preparation of the substrate.

The substrate structure and the lattice mismatch between the substrate and the layer to be deposited (epilayer) strongly influence the nucleation stage of growth, since they define the potential felt by the first layers of depositing species. The film and the substrate interaction play an important role in the thin film growth. Therefore, the substrate choice in thin film process is quite important. In this study, single crystal Si substrates are used. In heterostructure film growth, lattice mismatch to a large extend define the quality of the film grown, because large lattice mismatch will result in large defect density in the film. The lattice mismatch is defined as the difference between the lattice parameters of epilayer and the substrate.

This is calculated by

$$f_i = \frac{a_{si} - a_{ei}}{a_{ei}}, i = x, y \tag{2.1}$$

for cubic lattice where a is the bulk lattice constant, and e and s denote the epilayer and the substrate, respectively. A buffer layer is generally grown to compensate the large lattice mismatch.

The energy supplied to the growth surface determines, to a large extent, the microstructure and crystalline phase attained by the growing film. For example, if the energy available to the depositing species is low, this may result in low quality film since the low mobility of the atoms inhibit their movement to the optimal positions. Energy can be supplied to the surface in several ways, most importantly by the substrate temperature and the kinetic energy of the plasma species.

The content of the deposition flux is the main factor determining the composition of the film, but it can also influence the growth mechanisms, e.g., in deposition of compounds, growth can proceed by either single atoms or molecular units, depending on the specific deposition conditions. This can give rise to different bonding mechanisms and, consequently, structures of the grown films (Neidhart et al. 2003). However, it is not necessarily true that the grown film has the same composition, since the probabilities of gas phase scattering or sticking coefficient of the growing film may be different for different species. Still, the composition of the target is often transferred to the film, making sputtering of compound targets widely used for, e.g., metal alloy deposition.

2.2. Sputtering

Sputtering is one of the widely used physical vapor deposition techniques. This method is applicable both in industry and the research due to its advantages, such as low cost, high deposition rate and large area fabrication ability. In this work magnetron sputtering technique has been used to grow all the trilayer structures. In the following the sputtering deposition process is described in more detail.

2.2.1. Basics

The detailed picture of sputtering processes is rather complex, but the basic principles are straightforward (Ohring 2002): a target material is bombarded by accelerated ions, resulting in ejection (sputtering) of atoms/molecules from the target.

These atoms/molecules deposit onto the substrate and a film is formed. In thin film deposition, the source of the energetic ions is usually a low-pressure glow discharge or plasma (see next section), which is ignited and sustained between the target (cathode) and the substrate (anode) using a noble gas or mixture of noble gas with another gas (typically at a pressure of 1-100 mTorr). Basic sputtering system is illustrated in Fig. 2.1.

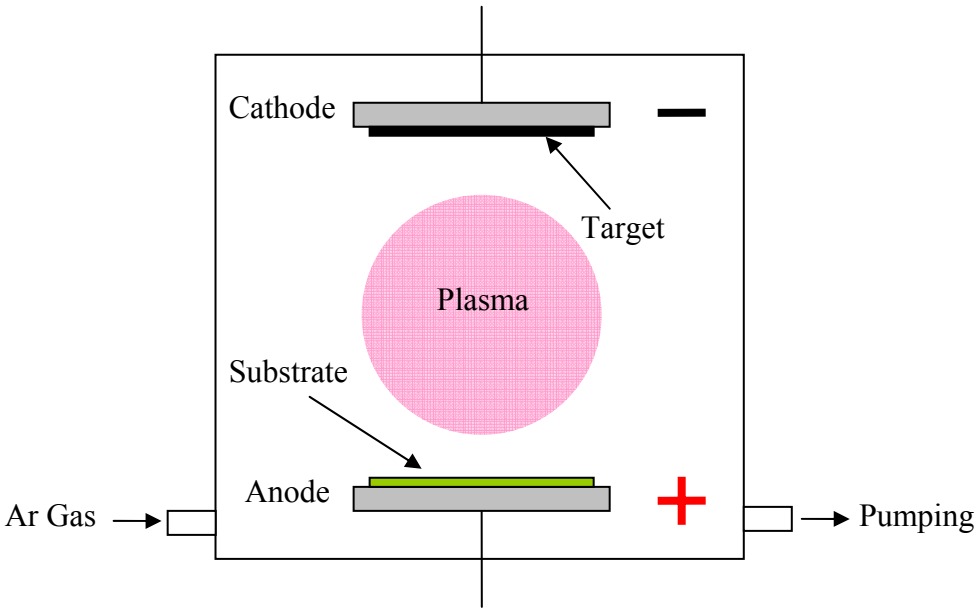

Figure 2.1. Schematic of a basic sputtering system.

As a high negative potential is maintained at the target, positive ions are accelerated from the plasma onto the target, causing sputtering. Two deposition parameters, both of which depend on the specific combination of process gas and target material, are critically important for the efficiency of the sputtering deposition process. These are the sputter yield and the secondary electron yield, i.e., the numbers of sputtered atoms and secondary electrons, respectively, which are produced per bombarding gas ion. The sputter yield e.g., the efficiency of momentum transfer, depends on the cross section of the collision, the binding energy of the target atoms, and the kinetic energy of the incoming ions. Sputter yield is denoted with, S, and is given by

$$S = \frac{\#\cdot of \cdot Emitted \cdot Particle}{\#\cdot of \cdot Incident \cdot Ion} \tag{2.2}$$

Table 2.1. Sputter yields of some materials for Ar^+ ion bombardment as function of ion energy. (Source: Ohring 2002).

Material	300 eV	500 eV	1000 eV
Ag	1.70	2.50	3.50
Al	0.60	0.90	1.50
Au	1.10	1.70	2.50
Cr	0.80	1.10	1.90
Cu	1.50	1.90	2.90
Fe	0.70	1.00	1.70
Ge	0.60	1.00	1.50
Ni	0.70	1.00	1.70
Si	0.30	0.70	1.00
Ti	0.30	0.50	0.70
Zn	3.70	5.00	7.00

In Table 2.1, the sputter yields of selected materials as a function of ion energy are summarized. A number of studies revealed that the crystal structure of the target considerably affects the sputter yield. Non-uniform angular dependencies of the sputter yield are reported in literature for single crystal targets while it shows a uniform character in polycrystalline targets.

The secondary electron yield is strongly dependent on the work function of the target material, i.e., high yield is achieved with low work function. At constant power, a higher electron yield results in a higher current drawn and, thus, lower discharge voltage and sputter yield. A higher yield also means a larger electronic fraction of the current and, hence, a lower sputter rate and ionic current. Therefore, a high secondary electron yield generally decreases the sputter efficiency.

2.2.2. The Plasma

Plasma is described as a partially ionized, but macroscopically neutral, gas containing neutrals, ions, and electrons, with high enough concentrations of charged particles for significant Coulomb interaction to occur (Chapman 1980). Another characteristic is a positive potential of the plasma (the plasma potential) relative to any surface in contact with it. This potential difference is caused by the higher velocities of

the electrons in the plasma compared to the ions, resulting in an initial negative charge build-up on the surface. The negative charge then tends to repel electrons and attract positive ions from the plasma until equilibrium is reached at a certain negative potential, relative to the plasma potential. The region between the plasma and an adjacent surface, over which the potential changes, is called the sheath. Sputtering plasma is sustained by applying a high (a few hundred volts) negative voltage to the target, which causes ions in the plasma to be accelerated over the sheath toward the target (Ohring 2002). The resulting collisions give rise to sputtering of target atoms and emission of secondary electrons. The electrons are accelerated toward the anode to ionize (by direct impact) more gas atoms, which bombard the target and produce more sputtered atoms and secondary electrons. When equilibrium is reached, a steady-state discharge is sustained and the ejected target atoms/molecules are deposited on the substrate and on the chamber walls also.

2.2.3. Magnetron Sputtering

Practically all sputtering processes today use magnetrons (Ohring 2002). The basic principle is to place permanent magnets behind the target to create a magnetic field between the outer and inner parts of the target, as schematically shown in Fig. 2.2. The electrons involved in the sputtering process are trapped in this field close to the target, where they dramatically increase the rate of ionization and thus the sputter rate. This can increase the deposition rate by an order of magnitude compared to non-magnetron sputtering. It also enables the use of lower pressures, which gives a more directional and energetic deposition flux due to less scattering of sputtered species. There is one drawback of magnetron sputtering which is a non-uniform consumption of the target because sputtering is focused in the area of highest electron density (the “erosion area”), i.e., where the magnetic field is parallel to the target surface.

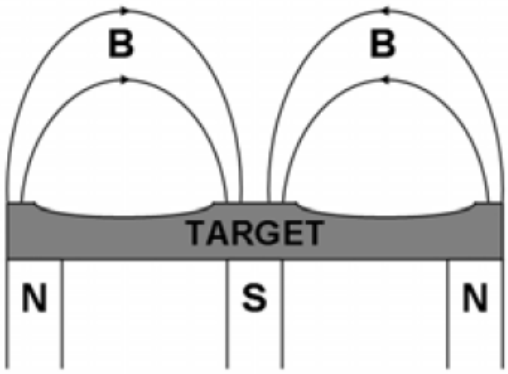

Figure 2.2. Schematic view of the magnetron cross-section and the erosion area formed on the surface of the target.

2.2.4. Radio Frequency Sputtering

Radio frequency (RF) power is commonly used to deposit insulating materials, which can be coupled through any target material, conducting or not. The frequency of 13.56 MHz, reserved by the Federal Communications Commission, is used as the power source. At this frequency the relatively heavy ions can not follow the oscillations, while the electrons can easily oscillate with the current (Ohring 2002). Therefore, they gain enough energy from the RF field to ionize the sputtering gas, reducing the need for secondary electrons to sustain the plasma and enabling lower operating pressures compared to DC sputtering. RF sputtering process is based on the fact that there is a self-biasing of the target to a negative potential of typically a few hundred volts. Due to this bias, the resulting sputtering process is quite similar to the case of DC sputtering. The self-bias is, in analogy with the plasma potential, explained by the much higher mobility of the electrons compared to the ions.

During a positive half-cycle of the oscillating RF voltage, a large negative (electron) current will be drawn on the target, but during the following negative half-cycle only a small positive (ion) current flows, due to the low mobility of the ions. Therefore, initially a net negative current is drawn into the target. Since no charge can be transferred through the capacitively coupled target a negative potential (the target self-bias) builds up until no net current flows. On the other hand, a matching circuit should also be used in RF sputtering to operate more efficiently because of the

impedance difference between the chamber and the power supply. One of the common impedance matching circuits can be seen in Fig. 2.3.

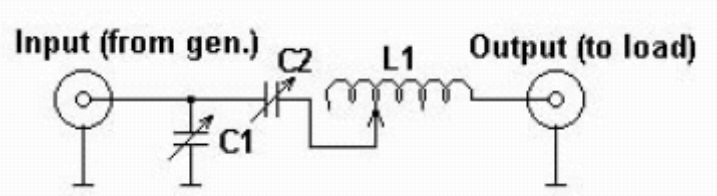

Figure 2.3. Typical impedance matching circuit.

2.2.5. Reactive Sputtering

When depositing compounds such as nitrides or oxides (e.g., TaO) by sputtering, it is not mandatory to use a compound target. In reactive sputtering, metallic targets (e.g., Ta) are used and a reactive gas (e.g., O_2) and a noble gas are mixed in the sputtering plasma. This extra gas reacts with the metal deposited on the substrate to form the intended compound film.

The reactive sputtering process is made complex by reactions occurring not only at the substrate (forming the film), but also at the target and the chamber walls, as described by the well established Berg model (Berg and Nyberg 2005). One of the important things in this type of sputtering is that the mixture of the reactive gas and the noble gas. This mixture ratio drastically affects the formed compound. In this work, 80% Ar + 20% O_2 mixture was used because this mixture amount results in the most stable form of Ta oxide which is the tantalum pentoxide (Ta_2O_5). For instance, using too much oxygen in the mixture can yield an oxidation of the target and thus the decrease in the sputter yield.

2.3. Material Properties

2.3.1. Iron (Fe):

Iron is a group VIII element and is a transition metal with a body-centered cubic (bcc) crystal structure shown in Fig. 2.4. Lattice constant of iron is 2.86 Å and the bulk

resistivity value is ~9.7 μΩ-cm. Iron is quite reactive with oxygen. Oxidation of iron is a challenging issue in thin film deposition since it may alter the ferromagnetism of the Fe film dramatically by creating magnetic dead layers at the interface.

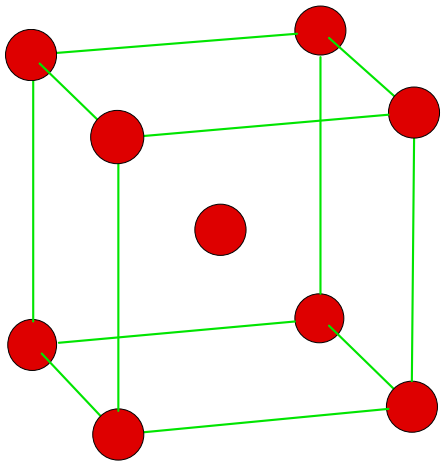

Figure 2.4. Crystal structure of bulk iron (BCC Cubic).

Fe is the best ferromagnet among three ferromagnetic transition metals in the elemental periodic table namely Fe, Co, Ni. The transition metals have 3d band which accommodates 10 electrons. Atomic Fe has four missing electrons in the 3d shell which result in ferromagnetism due to unpaired electrons. Coercivity of bulk iron is around ~20 Gauss (O'Handley 1999). Ferromagnetism is a pure quantum mechanical phenomenon and is explained by two effects: exchange splitting in the spin bands and the anti-bonding states between atoms. The density of states diagram of a normal metal is shown in Fig. 2.5 (a) where there are roughly equal number of spin up and down electrons. Fig. 2.5 (b) shows the density of states diagram of a ferromagnetic material. The splitting of density of states due to exchange field occurs within ferromagnets. Basic principle behind this splitting is the minimization of the total energy of the system. Therefore, the number of spin up and spin down electrons at the Fermi level is not equal. This result in creation of spin polarized current. Polarizability of bulk Fe is high (44 %) compared to Ni (31-33%) and Co (42%).

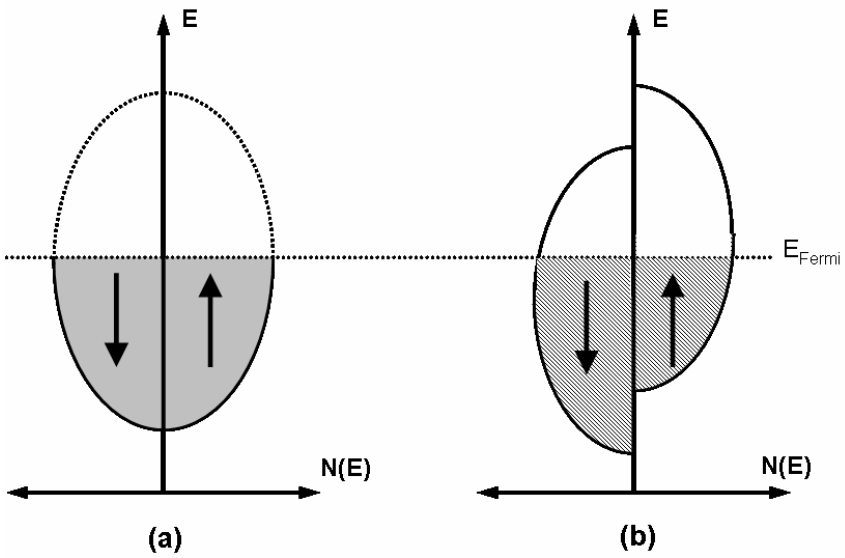

Figure 2.5. (a) Density of states of a normal metal and (b) spin splitting of the density of states in a ferromagnetic metal due to exchange field.

2.3.2. Tantalum (Ta) and Tantalum Oxide (TaO_x):

Tantalum is a group V element with a bcc crystal structure and lattice constant of 3.30 Å. Bulk resistivity of Ta is ~13 μΩ-cm. Tantalum is a widely used material in daily life. Some of its application areas are steel industry, medical applications, and electronics industry for use in capacitors.

Tantalum has three different compositions with oxides. Tantalum (II) oxide (TaO), tantalum (IV) oxide (TaO_2) and tantalum (V) oxide (Ta_2O_5) are the main oxides of tantalum. TaO and TaO_2 will not be discussed here but the latter one which is Ta_2O_5 will be the focus of this section.

Tantalum pentoxide is the most stable phase of the tantalum oxide. It consists of 18.1% oxygen and 81.9% tantalum in weight. It is a good dielectric material. Dielectric constant is between 20 and 30. Band gap of Ta_2O_5 is around 4.2 eV (for bulk Ta_2O_5) (Demiryont et al. 1985). Due to these properties, it has been studied as a gate oxide in CMOS research. Ta_2O_5 is a possible candidate to replace SiO_2 as a gate dielectric in electronics industry.

In the field of spintronics and magnetic tunnel junctions, there are few studies on tantalum oxide as a barrier material in MTJ structures. In this thesis, our aim is to grow tantalum oxide layer as a barrier material due to its low band gap and high dielectric

constant. Furthermore, tantalum oxide results in very low barrier height (~0.4 eV) (Gillies et al. 2001 and Rottländer et al. 2001). This low barrier height is quite advantageous in MTJs to have low resistance area (RA) product and also for a given resistance; it would allow reducing the ferromagnetic coupling over the barrier by increasing the barrier width.

2.3.3. Silicon (Si):

Silicon is the most abundant element in our earth and it is a semiconductor material. It has a diamond FCC lattice structure (Fig. 2.6) with lattice constant of 5.43 Å and energy band gap of 1.1 eV. Bulk resistivity of silicon is around 0.1 Ω-cm. Silicon is one of the most widely studied materials and is the basis of the whole electronics industry nowadays.

It has been used as a substrate material in this thesis because it has very low lattice mismatch (5.4 %) with the double iron lattice constant.

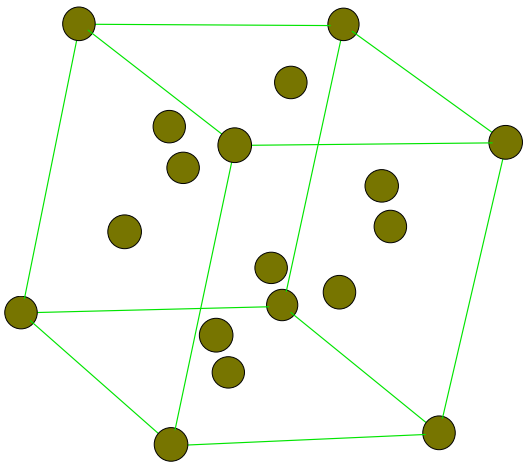

Figure 2.6. Crystal structure of silicon.

CHAPTER 3

EXPERIMENTAL

In this chapter, the experimental methods used to grow and characterize the layers will be discussed. The sample preparation and growth procedures will also be explained in detail. All layers were grown by magnetron sputtering. The crystallinity of the films and three layer structures were analyzed by X-ray powder diffraction (XRD) technique. Surface structures were studied by atomic force microscopy (AFM). The surface morphology, cross-section of the films and the elemental analysis were investigated by scanning electron microscope (SEM). Ellipsometry was used to find the refractive index and the Squid Magnetometer was used to obtain the hysteresis loops.

3.1. Magnetron Sputtering System

Sputtering technique is widely used as a thin film deposition technique in both industrial and research laboratories. This method is relatively cheap compared to other advanced techniques such as molecular beam epitaxy (MBE) and chemical vapor deposition (CVD). Sputtering technique is especially used to grow metal films, whereas MBE and CVD techniques were developed to grow basically semiconductors. Sputtering process simply involves ionization of noble gas atoms (typically Ar gas) and accelerating them onto a target by applying electric field. The impinging ions will remove target atoms by kinetic energy transfer. Removed target atoms will transfer the distance of 5 to 10 cm where a substrate is positioned and grow on it. In *magnetron* sputtering systems, electrons created within this process are trapped in a magnetic field to increase the ionizing probability. This raise in ionization increases the sputter yield. Therefore, growth rate of magnetron sputtering is higher compared to conventional sputtering systems. In a magnetron sputtering chamber, highly pure target materials are mounted on sputter heads. Mechanical shutters are placed on top of the heads: they can be positioned to start or stop the deposition as well as to grow multilayers without interrupting the growth process. Since sputtering process is low vacuum process (typically 1-100mTorr), pressure measurement requires capacitance manometers. On the other hand, depending on the electrical property of the target material, D.C. or R.F.

electric fields are used. For instance, insulating materials must be sputtered by using R.F. electric field because when insulating material is deposited on the substrate (anode) it will prevent current flow. Depending on the sputter system design, co-deposition of materials is also possible by using more than one head at the same time. By using different gases in the chamber, reactive sputtering can also be achieved.

All single layers and multilayers were grown in custom-made magnetron sputtering system in the Department of Physics at Izmir Institute of Technology (Fig. 3.1).

Figure 3.1. Photograph of magnetron sputtering system in Thin Film Laboratory.

The sputtering chamber is equipped with three magnetron sputter heads which can be tilted up to 45^0 located at the bottom of the chamber for sputter up orientation as illustrated in Fig. 3.2. Base pressure of the chamber is about $3x10^{-6}$ Torr. This high vacuum is achieved by a Turbo Molecular Pump. Plasma is created by using either DC or RF power supplies. Co-deposition of different materials is also possible in this system.

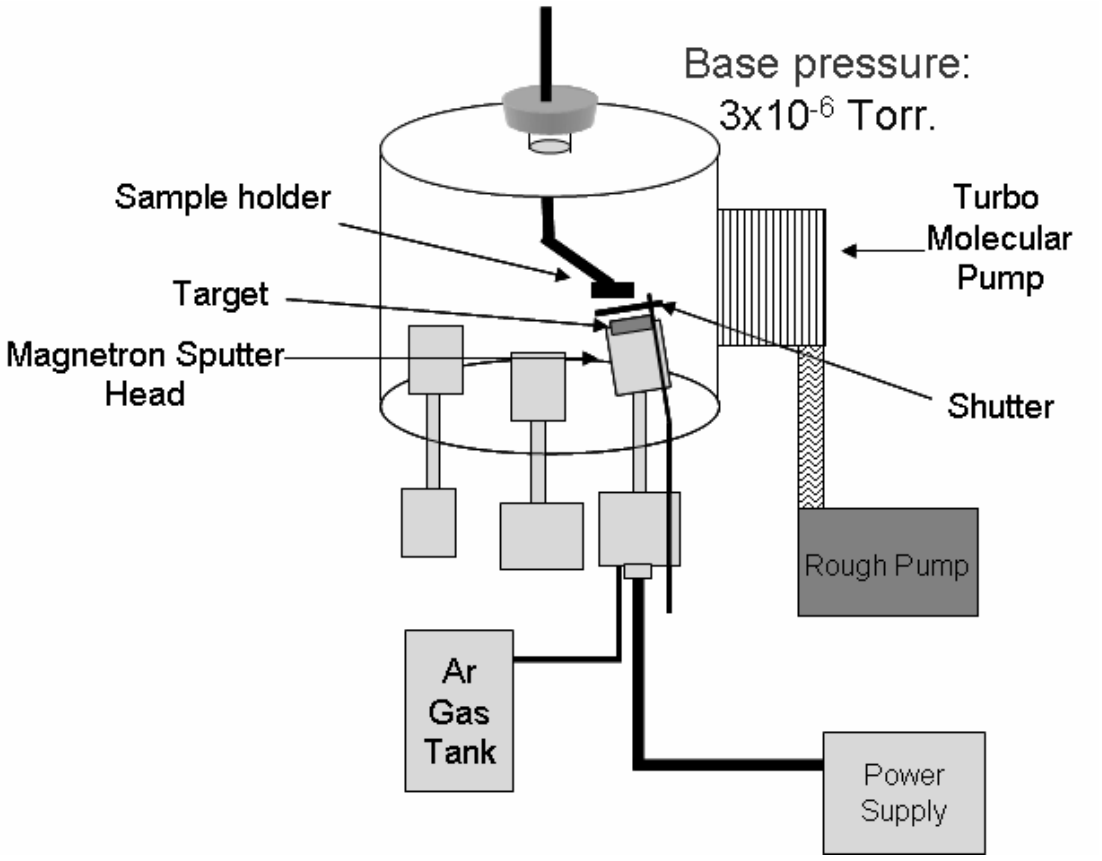

Figure 3.2. Schematic illustration of magnetron sputtering system in our laboratory.

3.2. Growth Procedure

3.2.1. Substrate Cleaning

N-type Si (001) oriented wafers with resistivity of 1-10 Ω-cm were used as substrates to grow the films. Chemical cleaning of the substrates was performed by using ultrasonic cleaner. Si wafer were first cleaned in ultrapure water for 10 minutes. This was followed by dipping it in methanol for 10 minutes and rinsing in ultrapure water. After drying by using nitrogen gas, substrates were loaded into magnetron sputtering system.

3.2.2. Film Deposition

All the layers in this thesis were grown at ambient temperature. First of all, single layers of iron, tantalum, and tantalum oxide were grown to study the structural properties of these films on Si substrate. We started with growing iron on Si (001) from a Fe target of 2" diameter and 0.100" thickness with the purity of 99.95%. Since iron is a ferromagnetic material, magnet configuration of the magnetron heads were changed as shown in Fig. 3.3 (b).

In magnetic configuration, magnetic field strength is reduced and directions of the magnetic field lines are changed. Iron has a large magnetic permeability therefore magnetic field lines are distorted and magnetic flux flows through iron target thus the plasma ignition is difficult. As a result, normal configuration is not suitable for deposition of magnetic materials.

Since our purpose is to grow thin films (10-100nm) we kept the substrate and target distance at 10 cm in order to have a slow growth rate. The growth rate is inversely proportional to the square of the target-substrate distance in sputtering. Before each iron deposition, target was subjected to pre-sputtering cleaning to remove oxide layer on the target surface. Pre-sputtering was performed at 20 W for 10 minutes and the target shutter was always kept closed during this process. Iron thin films were not heated during deposition because our system is not equipped with a substrate heating facility. Other deposition parameters for iron and all grown samples can be found in Table 3.1.

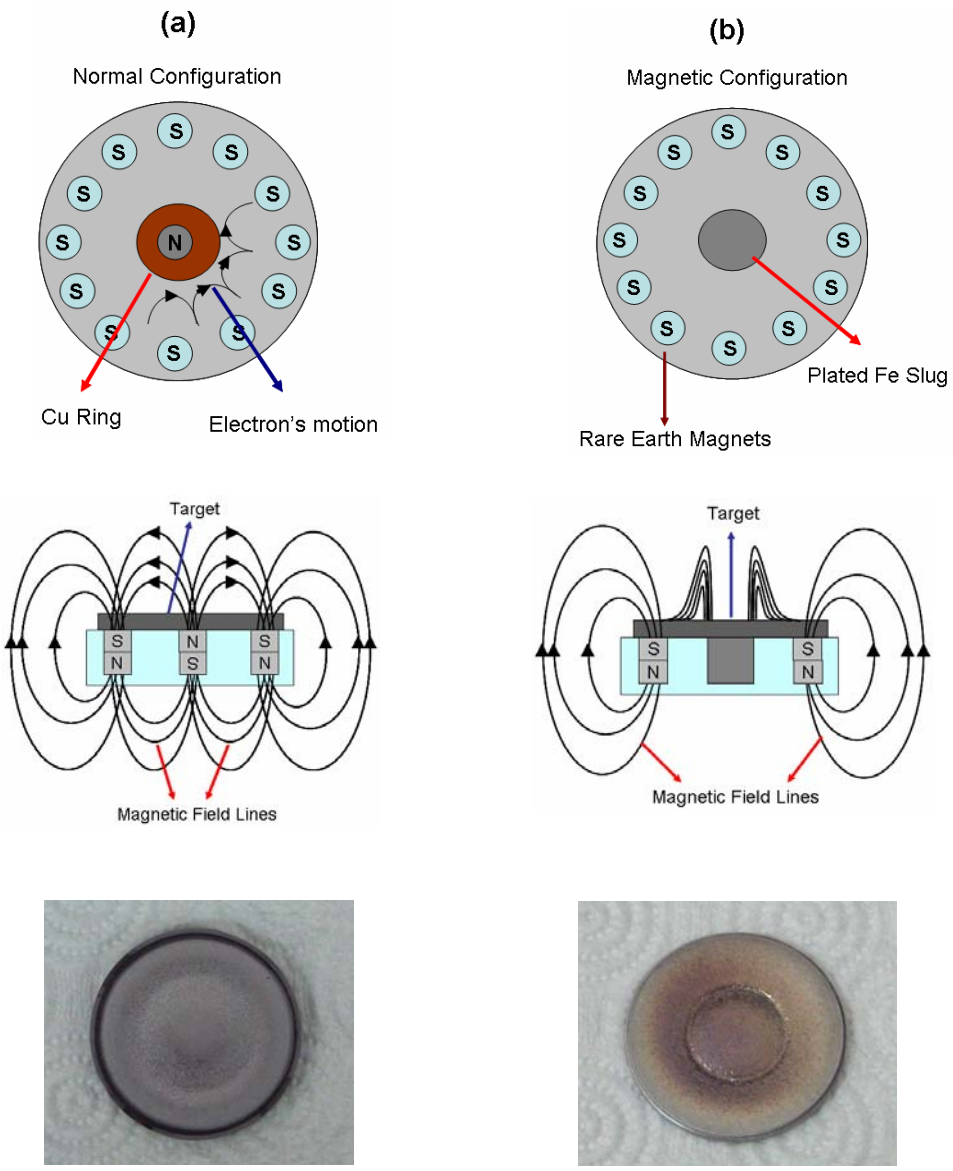

Figure 3.3. Schematic of magnet configuration and magnetic field lines of the magnetron heads for (a) non-magnetic materials (Ta target) and (b) ferromagnetic materials (Fe target).

After iron growth, thin (~200nm) tantalum single layer was grown on Si (001) substrates from a tantalum target (purity 99.95%) which have 2" diameter and 0.250" thickness. Tantalum was pre-sputtered in the same way with iron with Ar^+ ions before each deposition. Then, tantalum oxide was reactively sputtered on Si (001) substrates by using 80% Ar (purity 99.99%) and 20% O_2 (purity 99.99%) gas mixture. This gas composition was chosen based on the results in literature (Riekkinen and Molarius 2003). Pre-sputtering of Ta target was also performed before each tantalum oxide growth. Bi-

layers of Si(001)/Fe/Ta, Si(001)/Ta/Fe, Si(001)/Fe/TaO_x, and Si(001)/TaO_x/Fe were grown after optimizing the single layer deposition parameters. These bi-layers were deposited to have better understanding of the crystallization degree of each layer on top of another. After the analysis of bi-layers, multilayer structures such as Si(001)/Fe/Ta/Fe and Si(001)/Fe/TaO_x/Fe for different thickness values were grown.

Some of the multilayers were capped with very thin (~3-5 nm) gold layer by using Au target (purity 99.99%) in order to prevent oxidation of top iron layer. As-grown films were not exposed to any annealing procedure.

Table 3.1. Deposition conditions for all samples.

Sample Code, [Thickness (nm)]	**Power (W)**	**Growth Rate (Å/s)**	**Pressure (mTorr)**	**Gas Flow (sccm)**
Si(001)/Fe [220]	20	0.3	0.17	20
Si (001)/Ta [270]	20	0.5	0.53	20
Si(001)/TaO_x [70]	20	0.2	0.45	16 (Ar) + 4 (O_2)
Si(001)/Fe[220]/Ta[270]	20 for all	0.3 (Fe) 0.5 (Ta)	0.17 (Fe) 0.56 (Ta)	20 for both
Si(001)/Ta[270]/Fe[220]	20 for all	0.3 (Fe) 0.5 (Ta)	0.15 (Fe) 0.56 (Ta)	20 for both
Si(001)/Fe[220]/TaO_x[70]	20 for all	0.3 (Fe) 0.2 (TaO)	0.17 (Fe) 0.48 (TaO)	20 for (Fe) 16 (Ar) + 4 (O_2) for (TaO)
Si(001)/TaO_x[70]/Fe[220]	20 for all	0.3 (Fe) 0.2 (TaO)	0.18 (Fe) 0.52 (TaO)	20 for (Fe) 16 (Ar) + 4 (O_2) for (TaO)
Si(001)/Fe [220]/Ta [270]/Fe [220]	20 for all	0.3 (Fe) 0.5 (Ta)	0.17 (Fe), 0.5 (Ta)	20 for all
Si(001)/Fe [110]/TaO_x [70]/Fe [110]	20 for all	0.3 (Fe) 0.2 (TaO)	0.16 (Fe), 0.49 (TaO)	20 for (Fe) 16 (Ar) +4 (O_2) for (TaO)
Si(001)/Fe [50]/Ta [30]/Fe [50]/Au [5]	20 for all	0.3 (Fe) 0.5 (Ta) 0.8 (Au)	0.14 (Fe), 0.55 (Ta), 1.67 (Au)	20 for (Fe,Ta) 40 for (Au)
Si(001)/Fe [50]/TaO_x [35]/Fe [50]/Au [5]	20 for all	0.3 (Fe) 0.2 (TaO) 0.8 (Au)	0.13 (Fe), 0.51 (TaO), 1.68 (Au)	20 for (Fe), 16 (Ar) + 4 (O_2) for (TaO) 40 for (Au)

3.3. Characterization Techniques

3.3.1. X-Ray Diffraction (XRD)

X-ray diffraction (XRD) is a crystal structure determining technique. In this technique, diffraction of the X-rays occurs within the sample according to the Bragg's Law ($n\lambda=2d\sin\theta$) where λ is the X-ray wavelength, d is the layer separation and θ is the angle of incidence with the sample surface. Depending on the intensity, the position and the width of the diffraction peaks, the type and the quality of the crystal structure of the sample are determined.

Crystal structure is determined by analyzing the observed diffraction peaks. All of the planes do not give a diffraction peak in an XRD pattern. The crystal structure determines which diffraction peaks can be observed in the spectrum. For instance, $(h^2+k^2+l^2)$ should be even for BCC structures i.e., (110), (200), (211) planes and etc. gives diffraction peak in the XRD pattern. All of the known crystal systems give different diffraction planes. In fact, the reason for this is related to the structure factor calculations but this will not be discussed here. Comparison of the observed peaks with the known system provides to determine the crystal structure of an unknown sample.

The lattice constant of the film can also be determined by XRD. For instance for cubic structure, lattice parameter can be found by

$$a^2 = \frac{\lambda^2}{4\sin^2\theta}\cdot(h^2+k^2+l^2) \tag{3.1}$$

In the formula, a is the lattice constant (Å), λ is the X-ray wavelength (Å), θ is the diffraction angle and h, k, and l are the corresponding Miller indices. If the plane indices and the diffraction angle are found from the XRD spectrum, then lattice constant can easily be calculated using Eq. 3.1.

The FWHM (full width at half maximum) of an XRD peak is quite useful in XRD analysis. Fig. 3.4 shows the representation of FWHM of a possible XRD peak (a) and an ideal diffraction peak (b) in which the FWHM is zero.

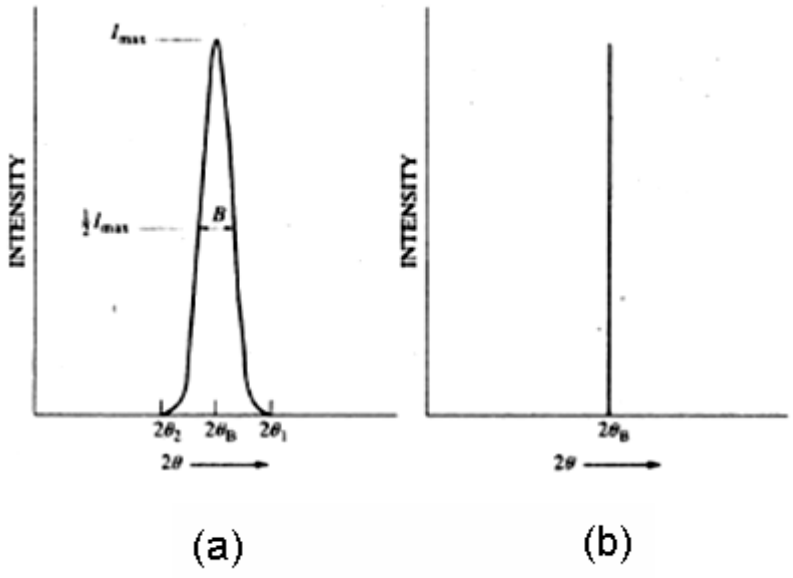

Figure 3.4. Full width at half maximum (FWHM) of a real (a) and an ideal (b) peak. (Source: Cullity and Stock 2001).

FWHM of a diffraction peak determines the crystalline quality of the film in XRD. Since FWHM represents how sharp that peak is, the smaller FWHM gives better crystallinity and the bigger grain sizes for that sample. FWHM is represented by *B* in X-ray diffraction and calculated roughly by;

$$B = \frac{1}{2} \cdot (2\theta_1 - 2\theta_2) \tag{3.2}$$

where $2\theta_1$ and $2\theta_2$ are the angles where the intensity of the diffraction peak drops to zero. FWHM of a peak must be determined by fitting. Gaussian model is generally used in fitting after background removal from the data. Grain sizes of the small crystals in the deposited film can be calculated by Scherrer's formula;

$$t = \frac{\lambda}{B \cdot \cos\theta_B} \tag{3.3}$$

where λ is the X-ray wavelength (Å), B is the FWHM of the diffraction peak (radians) and θ_B is the diffraction angle corresponding to that peak (Cullity and Stock 2001) .

Strain in the structure can also be studied in XRD by investigating the peak position and the FWHM. If the diffraction peak is just shifted towards left or right, then this means that there is a uniform strain in the epilayer. If the diffraction peak is both shifted and broadened, then the non-uniform strain is present within the grown film. The degree of the strain can be understood by looking at the shift and the broadening amount in the diffraction peak. XRD diffraction measurement is performed in two ways; one is the powder diffraction method and the other one is the grazing (low angle) incidence diffraction method. The latter one is applied to the thin film samples. When the incidence angle is very low (a few degrees), then X-rays does not penetrate to deep in the sample that means more signal comes from the film not from the substrate. θ and 2θ XRD scans can be performed depending on the diffractometer property.

In this study, X-ray powder diffractometer (Phillips X'Pert Pro) operating with Cu-Kα (1.54056 Å) radiation with Ni filter adjusted to 45 kV and 40 mA was used to determine the crystal quality of the films. Namely, the grain size and FWHM of selected samples were investigated after performing profile fittings of the diffraction peaks by Phillips X'pert Plus program. Lattice constant and strain in the structure were also found from these experiments. The XRD scans were performed in the 20-80° and 20-120^{o} 2θ ranges. For XRD measurements, thick (~300 nm) samples were grown. Multilayers and bi-layers were also investigated in the powder mode.

3.3.2. Atomic Force Microscopy (AFM)

Atomic force microscopy is a surface analysis technique based on the analysis of long range Van der Waals forces and repulsive forces. Atomically sharp Si based tip scans over the surface of a sample interacting with the surface in terms of atomic forces. The change in the height of the tip is gathered by using a laser directed onto it. Depending on the two dimensional height changes in the scan, a computer generates a surface image of that sample with a resolution of a few nanometers. This device works in two modes: 1) Contact mode and 2) Tapping mode. In contact mode, AFM tip is in contact with the surface during scanning process and the repulsive forces between tip and the surface are considered. On the other hand; in tapping mode, AFM tip oscillates at a fixed frequency and scans over the surface of the sample and the amplitude changes in the oscillation frequency is detected by very sensitive amplifiers. In this mode, long

range Van der Waals forces takes action between the tip and the surface of the material. Both methods have advantages and disadvantages. For instance, resolution of tapping mode is better than contact mode and this mode does not damage the sample surface whereas contact mode probably damages the surface during scan. But, contact mode gives better performance for big area scans (>100μm).

In this study, AFM measurements were performed by Multimode SPM, Nanoscope IV Digital Instrument device. Measurements were done both in contact and in tapping modes. In these modes, oxide-sharpened silicon nitride probes and etched Si probes were used, respectively. Sample size area of about 1 cm×1 cm was prepared. AFM was used for two purposes in this study: 1) Analysing the surface morphology and the roughness of the deposited films and 2) Defining the approximate thickness values of the individual films. 3x3 μm^2 areas were scanned for the surface analysis. Roughness measurements were performed on acquired images by using Nanoscope 5.12b48 analysis program. The thickness measurements were done by scratching the thin film grown glasses by very sharp needle and investigating step-height measurement on these samples. Analysis of captured images yielded thickness values for the corresponding sample.

3.3.3. Scanning Electron Microscopy (SEM) and Energy Dispersive X-ray (EDX) Analysis

Scanning electron microscopy (SEM) is a technique which can give high resolution (~20 nm) images of the samples. In this technique, electrons are created in a tube and are accelerated with several kV (1-30) potential differences. Accelerated electrons are directed onto the sample. The scattered electrons are gathered with various detectors like Back Scattered Electron (BSE) and Secondary Electron (SE) detectors. On the other hand, SEM includes an analysis called energy dispersive X-ray (EDX). This analysis can give local and global elemental composition of a sample. EDX detector is used to perform this analysis.

In this study, SEM (Phillips XL-30S FEG) was used to analyze the surface and the cross-section of the magnetic multilayers and to double-check the AFM thickness measurements. Moreover, EDX measurements were performed to investigate the elemental composition of the junctions. The oxygen content of the samples was

determined by EDX. In addition, the composition of tantalum oxide layer was analyzed by this method.

3.3.4. Ellipsometry

Ellipsometry is an optical technique which gives refractive index of materials. It is based on analysis of the interference of reflected beams from both film surface and the substrate surface. He-Ne laser (λ=633 nm) is generally used in the experiments. Analysis of the reflection data by applying some models, e.g. Cauchy model, produces refractive index and the thickness of the film under investigation.

In this thesis, Sentech SE801-E spectroscopic ellipsometry was used to find the refractive index and the thickness of the tantalum oxide single layer films on Si (001) substrate. Analysis was performed from 300 nm to 850 nm and Cauchy model was used for fitting.

3.3.5. SQUID Magnetometer

SQUID magnetometer is the most sensitive magnetic property measurement system. The sensitivity is typically around 10^{-8} emu.

In this study, Quantum Design MPMS XL-5 was used to obtain the hysteresis loops. Magnetic fields up to 5 Tesla can be applied by this system. M-T and R-T measurements can be accomplished from 4.2 K to 300 K also. Analysis of the samples was performed for ± 80 Oe at room temperature. Magnetic field was applied in the easy axis of Fe which is (100).

CHAPTER 4

RESULTS AND DISCUSSION

In this chapter, the data analysis of the characterization techniques will be explained. X-ray diffraction, atomic force microscopy and scanning electron microscopy results will be given respectively.

4.1. X-Ray Diffraction Results

Si/Fe:

Fig. 4.1 shows the XRD 2θ spectrum of Fe film on Si (001) sample which has the thickness of 220 nm. Fe (110) peak is clearly observed at 44.58 degrees with FWHM of 0.54^0 (1944 arcsec). FWHM of the peak was found by Gaussian fitting (Boubeta et al. 2003) as shown in the inlet of Fig. 4.1. This peak belongs to the iron body centered cubic (BCC) structure. There is no other diffraction peak related to other orientations of Fe in the spectrum indicating that Fe film is single crystal with average grain size of 17.5 nm. Scans for larger 2θ values were also performed but no diffraction peaks was observed other than Fe (110). Substrate peaks are also seen in the graph at 32.88^0 and 69.08^0 for (002) and (004) planes, respectively. We have observed crystalline structure for iron because of the small lattice mismatch (5.4%) between twice iron and silicon lattice parameters. Therefore, it can be concluded that iron grows well on silicon at room temperature in our magnetron sputtering system. It is reported that room temperature iron growth without substrate bias results in polycrystalline growth by sputtering (Yaegashi et al. 1994). On the other hand, no iron oxide related diffraction peak is observed in Fig. 4.1. The absence of iron oxides may be due to very thin layers, it is well known that Fe reacts with oxygen forming Fe-oxides. The grain size measurement was confirmed with the particle size analysis of AFM measurements. Lattice parameter was calculated as 2.872 Å from (110) peak at 44.58 degrees. This lattice constant is very close to the bulk lattice parameter which is 2.866 Å indicating there is no strain in the lattice.

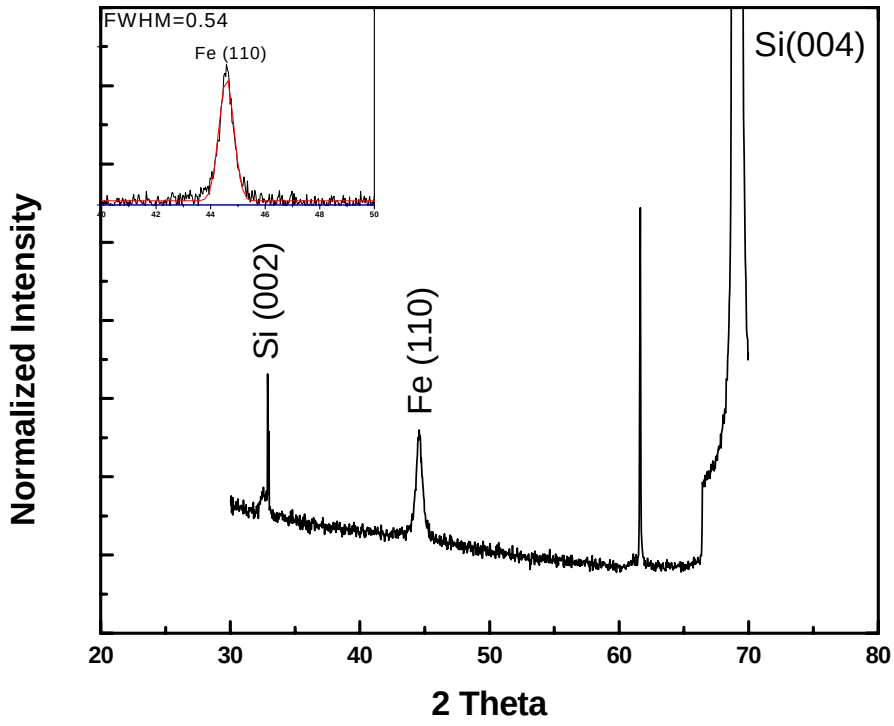

Figure 4.1. XRD pattern of Fe on Si (001) with 220 nm thickness. In the inlet fitted Fe (110) peak is shown.

As a reference, Fig. 4.2 illustrates the XRD spectrum for Fe sputter target that was used in this thesis. 2θ scan was performed for the target and it is observed that our sputter target is polycrystalline. In the spectrum, (110), (200), (211), and (220) planes of BCC iron can easily be seen. FWHM of (110) peak is found to be 0.11^0.

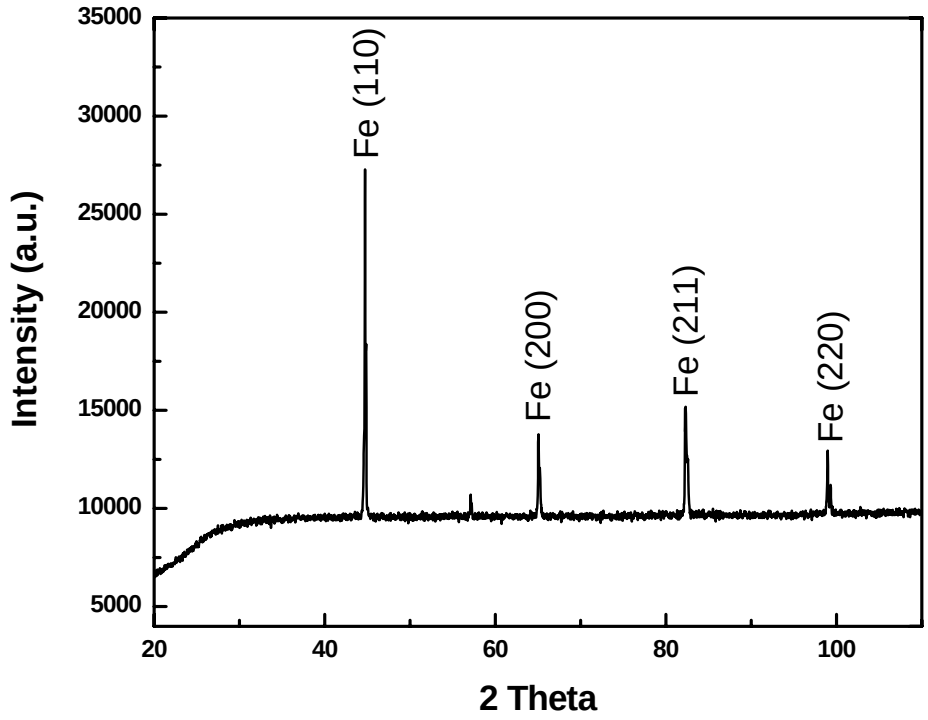

Figure 4.2. XRD diffraction spectrum of Fe sputter target.

Table 4.1. FWHM of (110) diffraction peaks and grain sizes of iron and tantalum in single layer, Si/Fe/Ta and Si/Fe/Ta/Fe samples, respectively and FWHM and grain size for silicon substrate and Fe (200) peak in multilayer structure.

	FWHM (Degree)		**Grain Size (nm)**	
	Fe (110)	**Ta (110)**	**Fe (110)**	**Ta (110)**
Single Layer	0,54	3,89	17,5	2,3
Si/Fe/Ta	0,55	0,72	17,2	13,9
Si/Fe/Ta/Fe	0,58	0,77	17,7	13,3
Fe (200) Peak in Si/Fe/Ta/Fe	1,02		16,2	
Substrate (Si)	0,06		151,4	

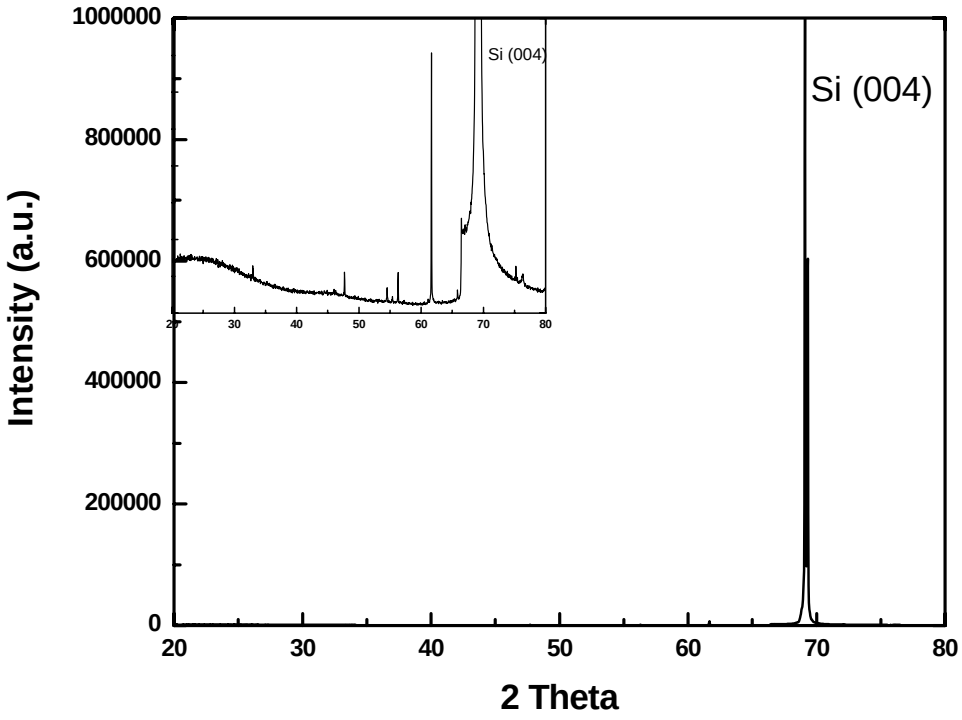

Figure 4.3. XRD pattern for Si (001) substrate. Inlet shows the zoomed pattern.

Fig. 4.3 shows XRD spectrum for single crystal Si (001) substrate. Si (004) peak can be seen at 69.1 degrees with very high intensity. The other peaks are not seen in the figure due to the high intensity of (004) diffraction peak. But inlet of Fig. 4.3 illustrates the other peaks related to silicon substrate. The (004) diffraction peak has 0.06^0 FWHM and average grain size of the crystallites was calculated to be ~151 nm.

Si/Ta:

XRD pattern for Ta growth (270 nm) on Si (001) is shown in Fig. 4.4. In this scan, we can distinguish BCC Ta (110) peak at 37.29^0 but this peak is quite broad and has low intensity. FWHM of the peak was found to be 3.89 degrees.

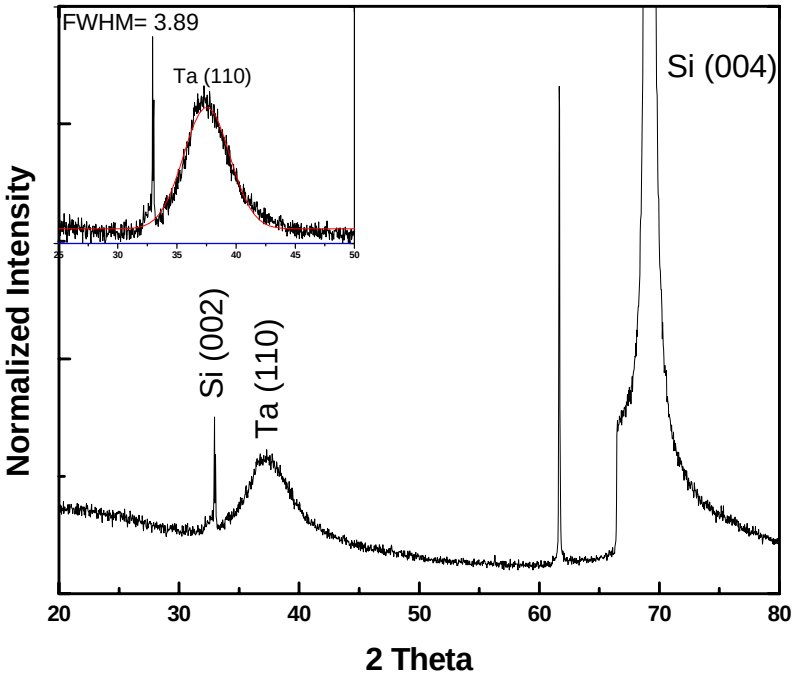

Figure 4.4. XRD pattern for Ta growth on Si (001) with 270 nm thickness. In the inlet, fitting of Ta (110) peak is illustrated.

One of the reasons of poor crystallinity of tantalum film might be the large lattice mismatch (21%) between twice tantalum and silicon lattice constants. Bulk tantalum has BCC cubic structure and silicon has diamond FCC structure. The lattice structures of the two films could also be another reason for the observed diffraction pattern. Grain size of crystallites and the lattice constant of tantalum were calculated as 2.3 nm and 3.401 Å (Table 4.1), respectively from the fitted curve shown in the inlet of Fig. 4.4. Moreover, the 1.19 degree shift to left and broadening in the (110) peak indicate the existence of residual tensile stress in the film. This stress causes lattice to extend by 3%.

Si/TaO_x:

The XRD scan of reactive sputtering of TaO_x is illustrated in Fig. 4.5. Only substrate diffraction peaks are observed in the figure. An amorphous structure is obtained for tantalum oxide growth. It is reported that room temperature deposition of tantalum oxide results in amorphous films (Dimitrova et al. 2001 and Platt et al. 1997). Annealing in O_2 atmosphere (Dimitrova et al. 2001), rapid thermal annealing in N_2 atmosphere (Ezhilvalavan and Tseng 2000) or high temperature (493^0 K) growth

(Dimitrova et al. 2001) results in crystallization of tantalum oxide. It is claimed that insulating properties of tantalum pentoxide are increasing with the crystallization (Chaneliere et al. 1999). Thus, it is desired to have crystal tantalum pentoxide as a barrier in magnetic multilayers. Amorphous tantalum pentoxide has the problem of conduction through pinholes in studies of magnetic tunnel junctions (Platt et al. 1997).

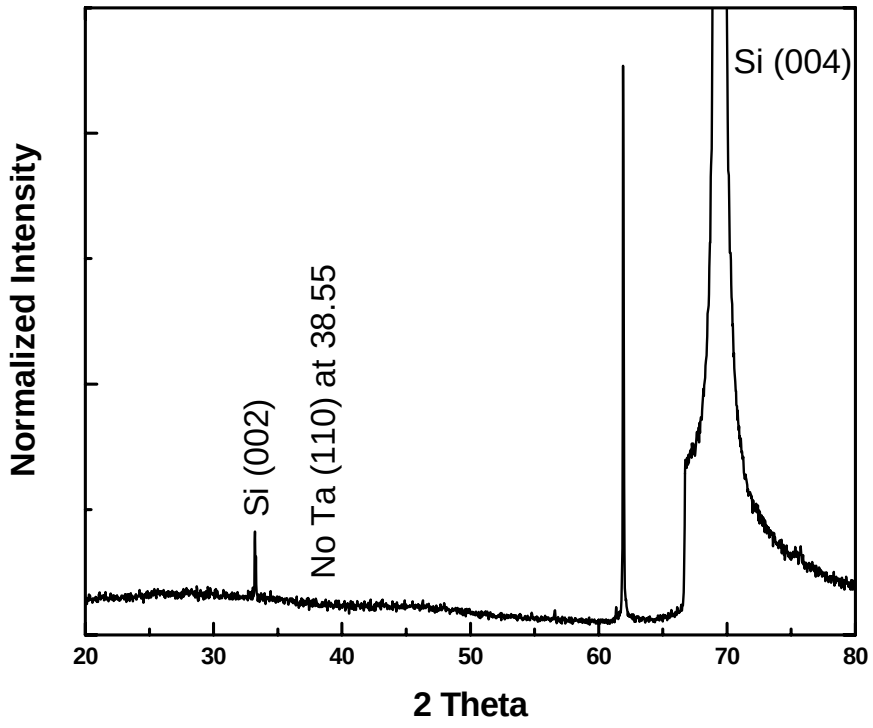

Figure 4.5. XRD pattern for TaO_x on Si (001) which has the thickness of 70 nm.

Si/Fe/Ta, Si/Ta/Fe, Si/Fe/Ta/Fe:

After XRD analysis of single layers of Fe, Ta and TaO, bilayers of Fe/Ta, Ta/Fe, Fe/TaO and TaO/Fe were grown on Si (001) substrate. Fig. 4.6 shows XRD analysis of Si/Fe (220 nm)/Ta (270 nm), Si/Ta (270 nm)/Fe (220 nm) and Si/Fe (220 nm)/Ta (270 nm)/Fe (220 nm) bilayers and multilayer, respectively. Diffraction patterns were obtained for 20-80 2θ range. In the figure, Fe (110), Ta (110), Fe (200) and substrate peaks are observed clearly. For Si/Fe/Ta sample; Ta (110) is quite sharp and has high intensity with FWHM of 0.72^0 and grain size of 13.9 nm because iron and tantalum has the same structure and the lattice mismatch is low (13%) compared to silicon-tantalum

interface (21%). Iron exhibits crystalline structure in this sample with Fe (110) peak formation with 0.55^0 FWHM and 17.2 average grain size as summarized in Table 4.1.

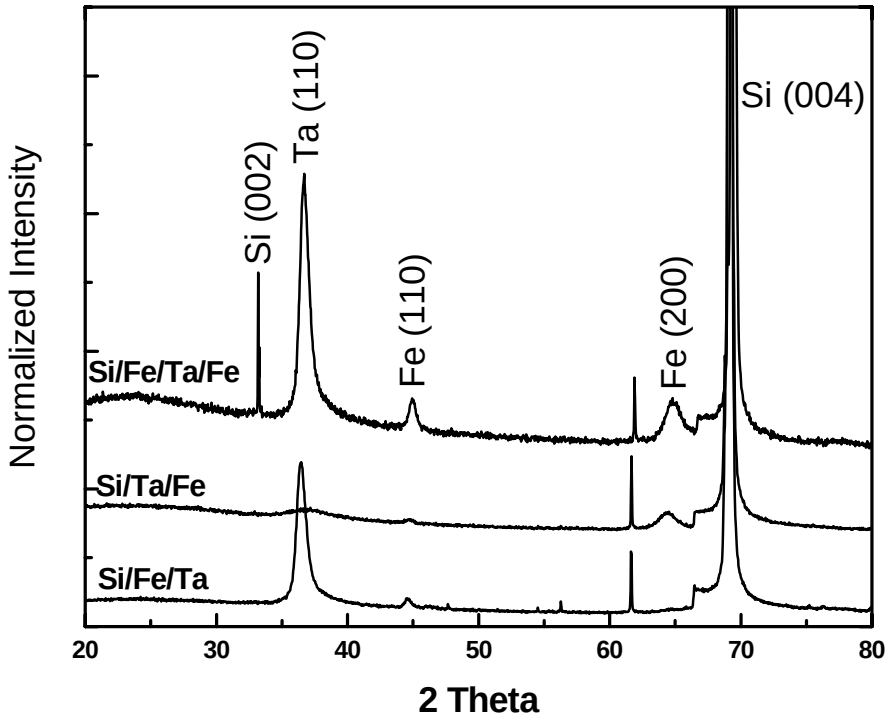

Figure 4.6. XRD diffraction patterns of Si/Fe/Ta, Si/Ta/Fe and Si/Fe/Ta/Fe bilayers and multilayer, respectively.

On the other hand, in Si/Ta/Fe sample, Fe (110) peak was also observed but it has very low intensity. Fe (200) peak formation with 1.02^0 FWHM and 16.2 nm grain size (Table 4.1) was observed at 64.53^0 in this bilayer configuration. Ta (110) is hardly distinguished and very broad due to the large lattice mismatch (21%) with silicon as discussed before. In Si/Ta/Fe sample we observed that Ta grows very well on Fe but from the basics of growth it is clear that if one material grows well on another, vice versa will not be same quality. Therefore, low quality iron film with (200) orientation was observed in Si/Ta/Fe sample where iron was grown on tantalum layer.

When we compare bilayers with Si/Fe/Ta/Fe multilayer spectrum, expected situation was observed as can be seen in Fig. 4.6. In the graph, Fe (110), Fe (200) and Ta (110) peaks were clearly distinguished. Tantalum exhibited a good crystalline quality with FWHM of 0.77^0 and grain size of 13.3 nm for (110) peak. On the other hand, two iron diffraction peaks were observed which were (110) and (200) planes with

0.58^0 and 1.02^0 FWHM values, respectively. This second peak formation of Fe is devoted to the top iron layer in the sample as discussed above.

Si/Fe/TaO_x, Si/TaO_x/Fe, Si/Fe/TaO_x/Fe:

XRD diffraction pattern of Si/Fe (220 nm)/TaO_x (70 nm), Si/TaO_x (70 nm)/Fe (220 nm) and Si/Fe (110 nm)/TaO_x (70 nm)/Fe (110 nm) bilayers and the multilayer were illustrated in Fig. 4.7. In the figure, Si/Fe/TaO_x sample shows only Fe (110) peak along with substrate peaks. Tantalum or tantalum oxide related diffraction peaks are not present in the spectrum indicating amorphous TaO_x film on Fe.

From Si/TaO_x/Fe sample, same peak (110) is observed for iron and tantalum oxide is amorphous again but a higher intensity Fe (110) peak is observed. Graph of multilayer (Si/Fe/TaO_x/Fe) exhibits quite different spectrum. Here two diffraction peaks are observed for (110) and (200) planes of iron, respectively.

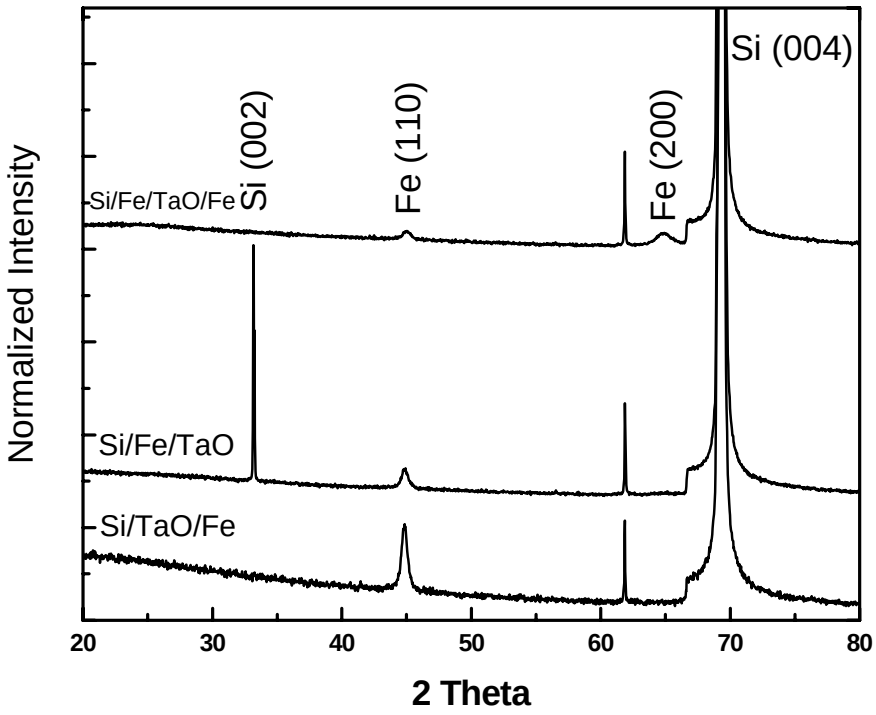

Figure 4.7. XRD spectra of Si/Fe/TaO_x, Si/TaO_x/Fe and Si/Fe/TaO_x/Fe bilayers and the multilayer, respectively.

Moreover, Fe (110) peak has lower intensity than Si/Fe/TaO_x and Si/TaO_x/Fe samples. This is most probably because of the thickness difference in multilayer. We have 110 nm iron layers in multilayer structure. Second peak formation for iron may be explained with the interaction between TaO_x and top iron electrode. As shown in Fig. 4.7 second layer of Fe on TaO_x results in diffraction peak of (200). Since we know that iron grows in (110) orientation on Si, (200) peak formation can be a result of the interaction of the top electrode. It is attained by the Fe layer on Ta rich TaO_x surface.

Si/Fe/Ta/Fe and Si/Fe/TaO_x/Fe (Thin Samples):

In addition to thick junctions, XRD scans for thinner junctions like Si (001)/Fe (50nm)/Ta (30nm)/Fe (50nm)/Au and Si/Fe (50nm)/TaO (35nm)/Fe (50nm)/Au were also performed. Their diffraction patterns can be seen in Fig. 4.8 and 4.9, respectively.

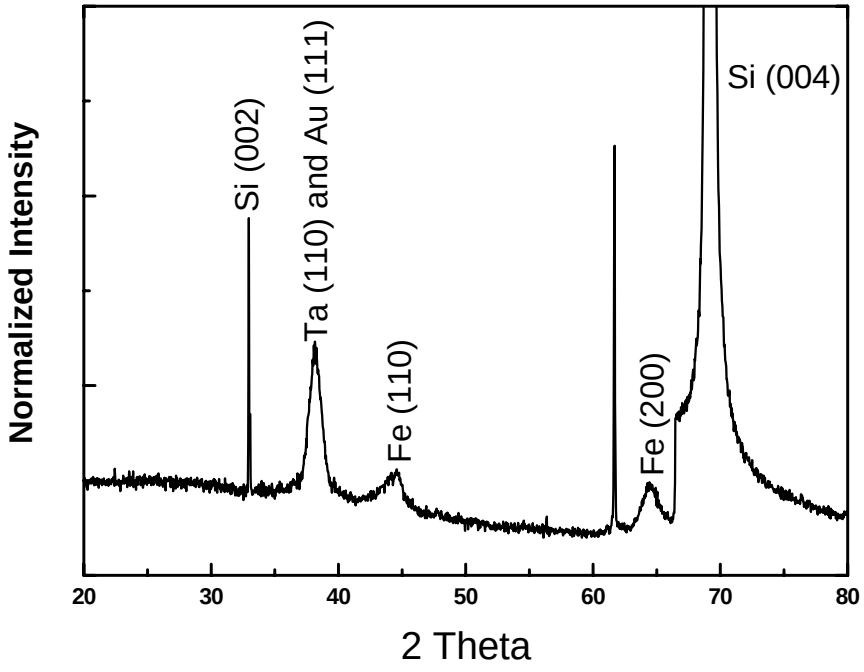

Figure 4.8. XRD scan for Fe (50nm)/Ta (30nm)/Fe (50nm)/Au (~5nm) on Si (001).

In these thin samples, the same behaviors with thick ones are observed whereas intensities of the diffraction peaks are lower than those which are thick. In addition, XRD patterns showed Au (111) peak at 38.10^0 since these samples were capped with very thin (~5 nm) gold layer.

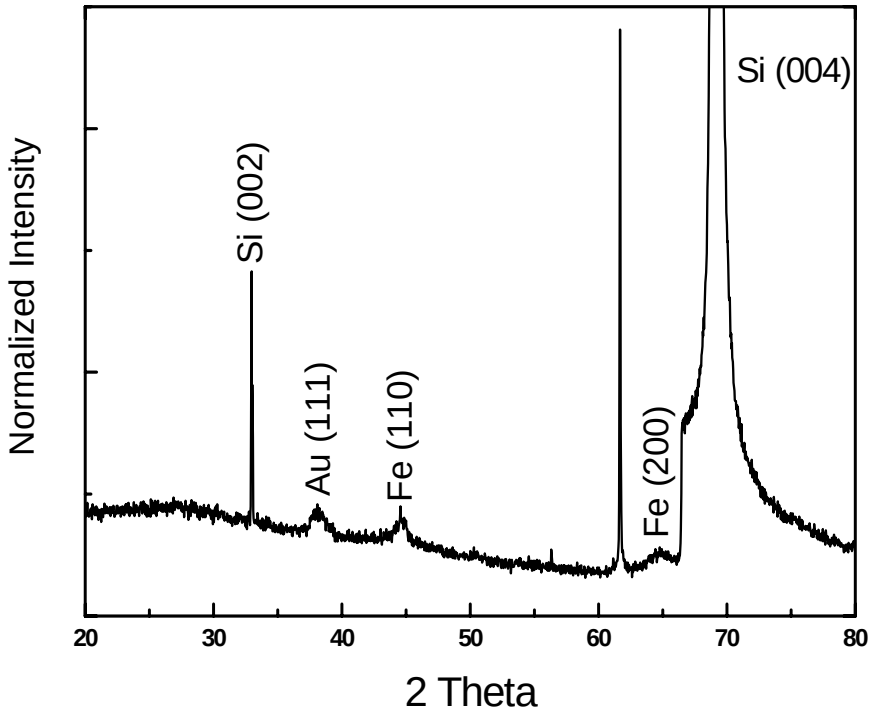

Figure 4.9. XRD scan for Fe (50nm)/TaO_x (35nm)/Fe (50nm)/Au (~5nm) on Si (001).

4.2. Atomic Force Microscopy Results

AFM surface measurements for silicon substrate, iron and tantalum on Si (001) substrates are shown in Fig. 4.10- 4.13, respectively. All surface images were taken for 3x3 μm^2 areas. Average roughness values for all samples are summarized in Table 4.2.

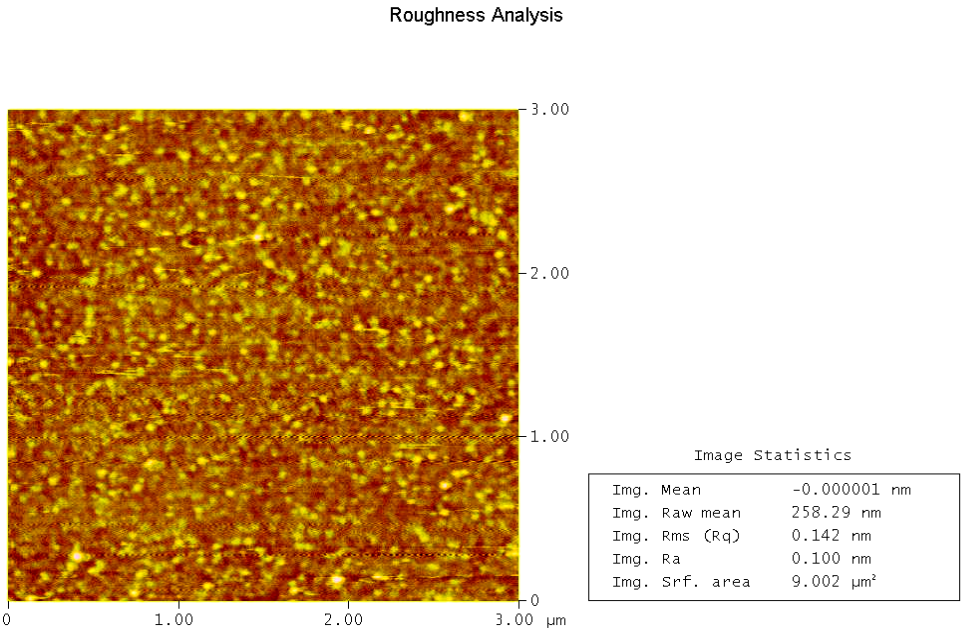

Figure 4.10. Roughness analysis of Si (001) substrate.

The silicon substrate has 0.12 nm average surface roughness which is expected for a single crystal substrate as can be seen in Fig. 4.10. Small granular (less than 60 nm) structures were observed on the surface. These structures might be a result of native oxide formed on the surface of silicon because bigger grains are expected for a single crystal substrate. We expect grain sizes of the substrate to be ~151 nm which are found from the XRD analysis.

Table 4.2. Average roughness values for Si substrate, Fe, Ta and TaO_x single layers and Ta and TaO_x films on Fe. Measurements were repeated for 4 different places on the surfaces and averaged.

Sample	Roughness (nm)
Si Substrate	0.12
Fe on Si (001)	0.2
Ta on Si (001)	0.3
TaO_x on Si (001)	1.1
Ta on Fe/Si (001)	0.9
TaO_x on Fe/Si (001)	0.2

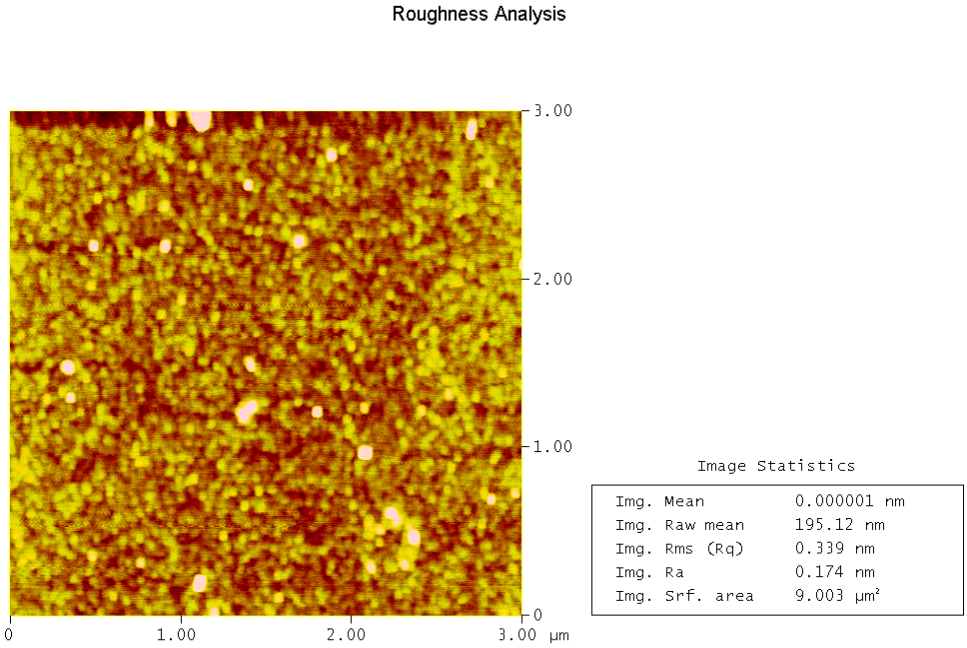

Figure 4.11. Roughness analysis for Fe on Si (001).

Surface morphology of the iron film on silicon is illustrated in Fig. 4.11. 0.2 nm average roughness was found for the iron film. This means that iron film is quite smooth and uniform on silicon where it has 0.12 nm average roughness. Average grain size of 15 nm has been found from particle analysis of this image and this is in good agreement with the grain size calculated from XRD analysis which is 17.5 nm.

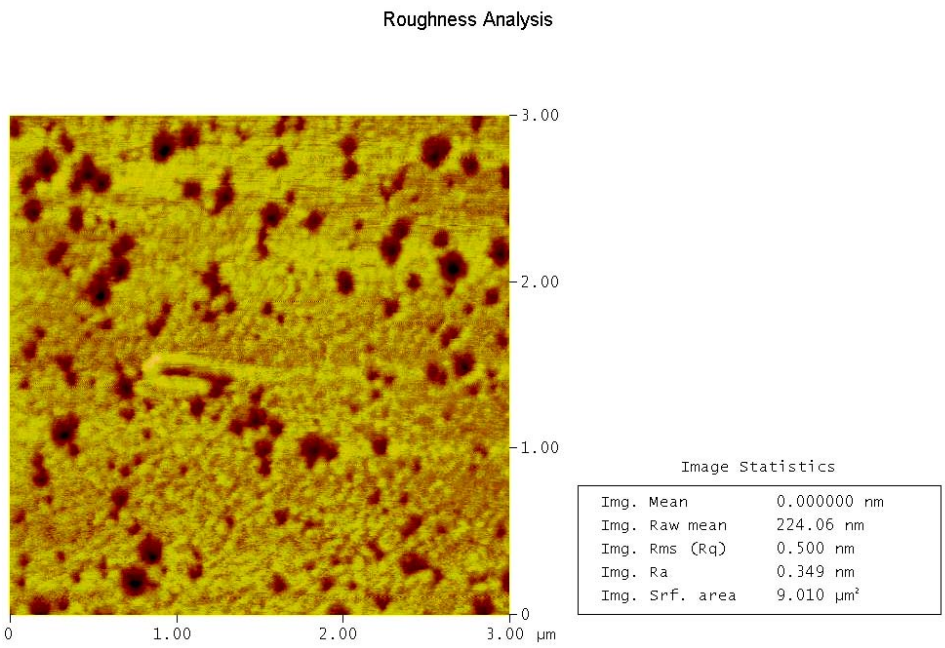

Figure 4.12. Roughness analysis for Ta on Si (001).

Fig. 4.12 shows the surface morphology of tantalum layer on Si (001) substrate. In the image, granular structure of tantalum with 0.3 nm average roughness can be observed. In addition, there are some kinds of low height points (darker points). These points have average depth of 2-3 nm. In the image they seem to be deeper because of the vertical scale (Z direction). But it seems that tantalum surface has some non-uniformity which results in 0.3 nm roughness. We have seen that our tantalum film has low crystal quality on silicon due to large lattice mismatch. On the contrary, the low quality tantalum film exhibits smooth surface on silicon.

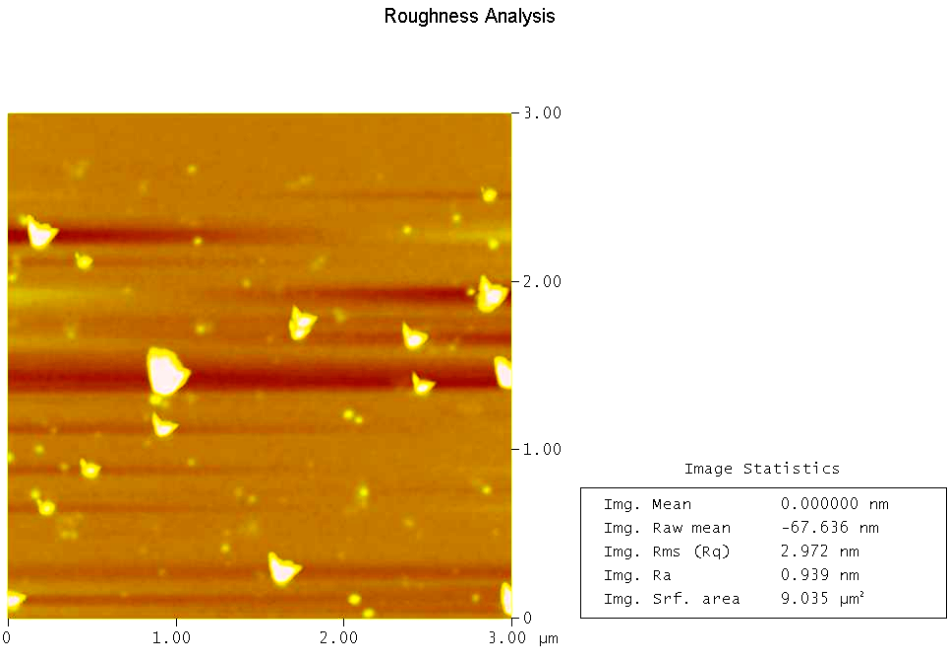

Figure 4.13. Roughness analysis for TaO_x on Si (001).

Surface morphology of the TaO on Si (001) sample can be observed from Fig. 4.13. It seems that TaO_x grows very rough on silicon substrate with 1.1 nm average roughness. Big particles were observed on the surface of tantalum oxide. Particles have 20-30 nm average height which mainly causes the roughness of the surface. In addition, these particles were also noticed in SEM cross-section micrographs. Amorphous structure of tantalum oxide may be the reason for these particles. In literature, smoother surfaces of tantalum oxide were grown with high substrate temperatures. Moreover, average roughness values increase with the higher substrate temperature (Nishimura et al. 1998). In our deposition, we did not heat the substrate but surface roughness may be improved by growing at high substrate temperatures.

As can be observed from Table 4.2 and Fig. 4.11-4.13, iron single layer has lower average surface roughness value than tantalum and tantalum oxide. On the contrary, single tantalum oxide layer exhibits the highest average surface roughness with 1.1 nm because TaO_x film is totally amorphous. The other films were comparably smooth.

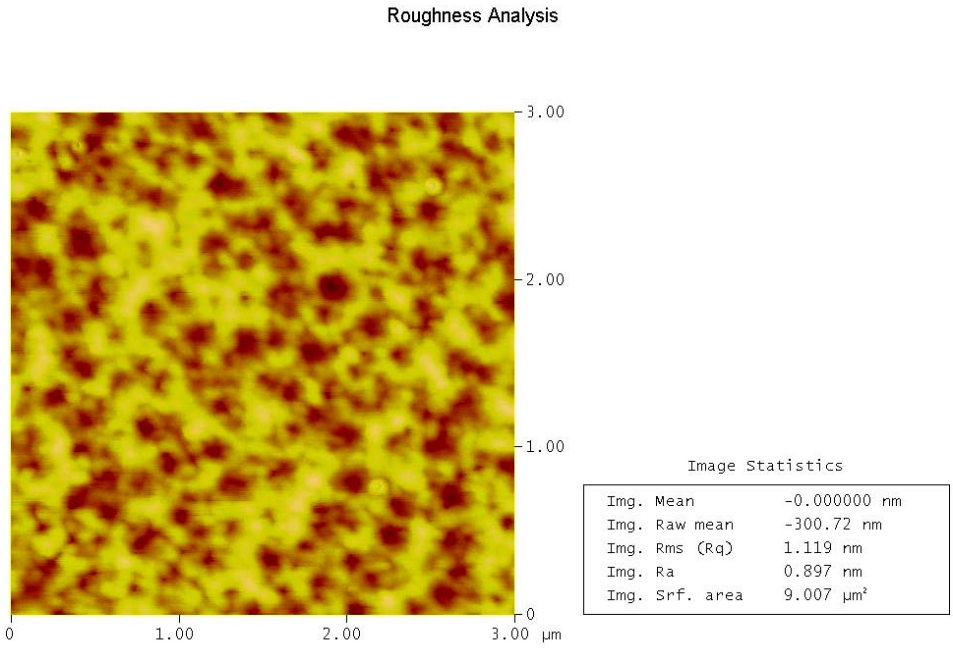

Figure 4.14. Roughness analysis for Ta on Fe/Si (001).

Fig. 4.14 shows roughness measurement for Si (001)/Fe (220 nm)/Ta (270 nm) sample. Average roughness for this sample was calculated to be 0.9 nm and this is quite rough compared to single Ta layer on silicon which has 0.3 nm roughness. Image illustrates that we have uniform tantalum layer on iron. In addition, dark points are not present in this sample this is because tantalum grows well on iron because they have similar lattice structure as well as small misfit. The other way around, Ta/Fe, Fe on Ta does not grow well because of the surface energies are reversed.

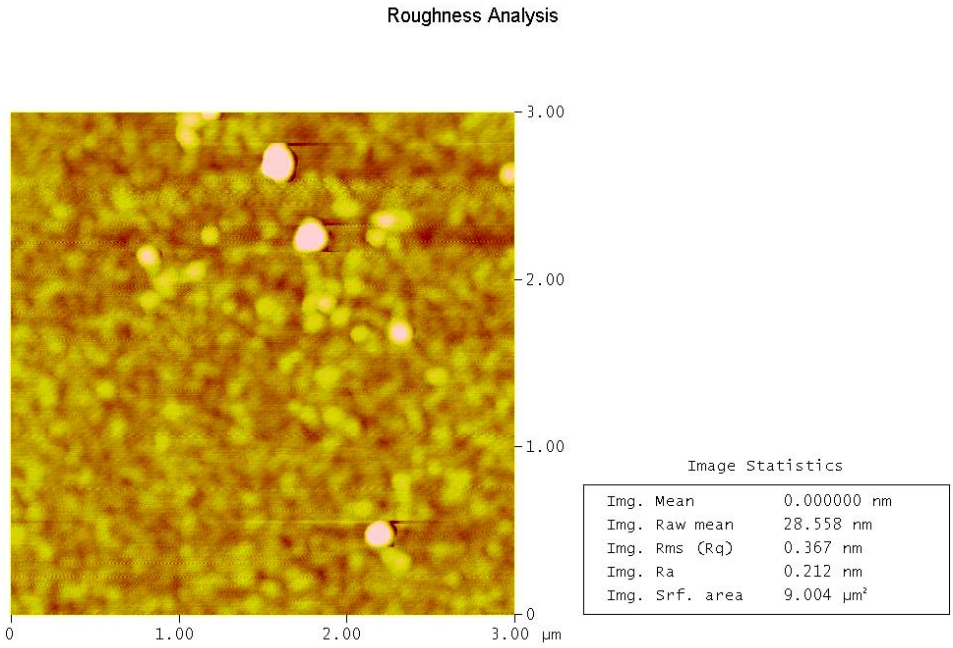

Figure 4.15. Roughness analysis for TaO_x on Fe/Si (001).

Roughness analysis for TaO_x on Si (001)/Fe is shown in Fig. 4.15. From the obtained surface images, average roughness was found to be 0.18 nm which is much lower than single TaO_x layer on silicon. This was one of our aims to have very flat surfaces of barrier layer in between two ferromagnetic electrodes. Roughness of the barrier directly affects the crystal quality of the top electrode and it may degrade the crystal quality. Furthermore, it might result in magnetic dead layers at the interface. The granular structure is observed from the image and we have some big particles on the surface but these are not as big as the ones on the single layer of tantalum oxide on silicon. Grain sizes on this sample are found to be 11 nm by the particle analysis in AFM program.

4.3. Scanning Electron Microscopy Results

Fig. 4.16 illustrates the SEM cross-section image of Fe (220nm) on Si (001) sample. Iron layer on Si can easily be observed from this image. The top bright layer is the thin gold capping layer on the sample. Thickness of the iron layer was found to be 220 nm from this micrograph. This thickness value is in good agreement with AFM measurements. Moreover, uniform deposition of iron on silicon substrate can also be clearly noticed in Fig. 4.16.

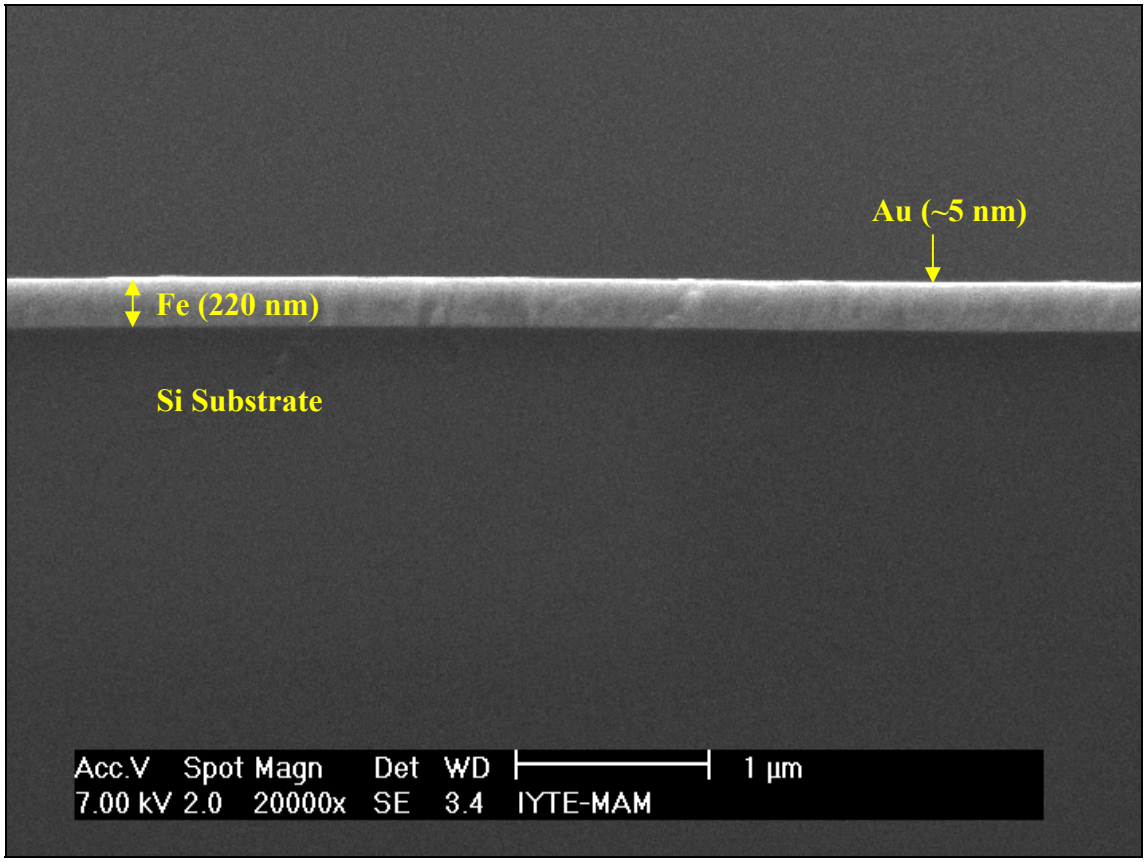

Figure 4.16. SEM cross-section micrograph of gold capped Fe (220 nm) on Si (001).

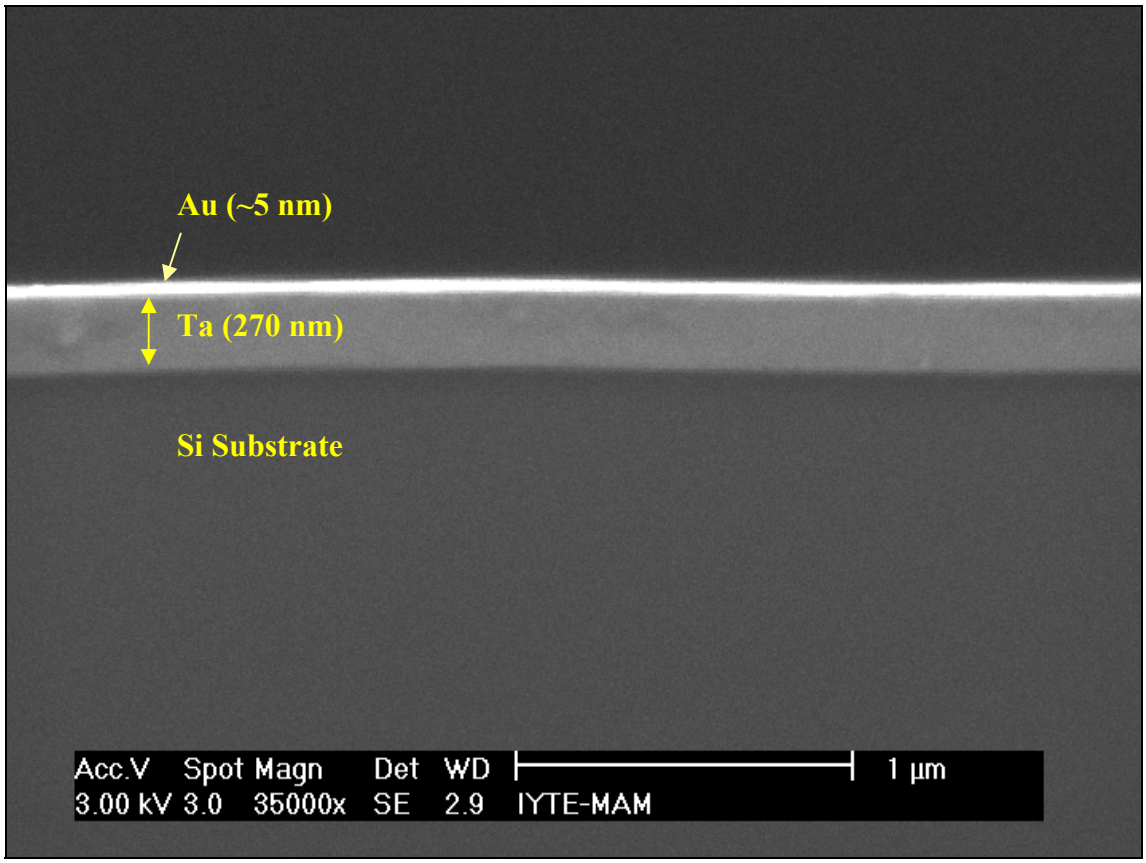

Figure 4.17. SEM cross-section micrograph of gold capped Ta (270 nm) on Si (001).

Cross-section of tantalum single layer on Si (001) is illustrated in Fig. 4.17. The top layer is again very thin gold. Uniform tantalum and continuous deposition can be seen from the micrograph. Thickness of the film was found to be 270 nm which is similar to the AFM measurement results. Intermixing at the interface was not observed at this scale.

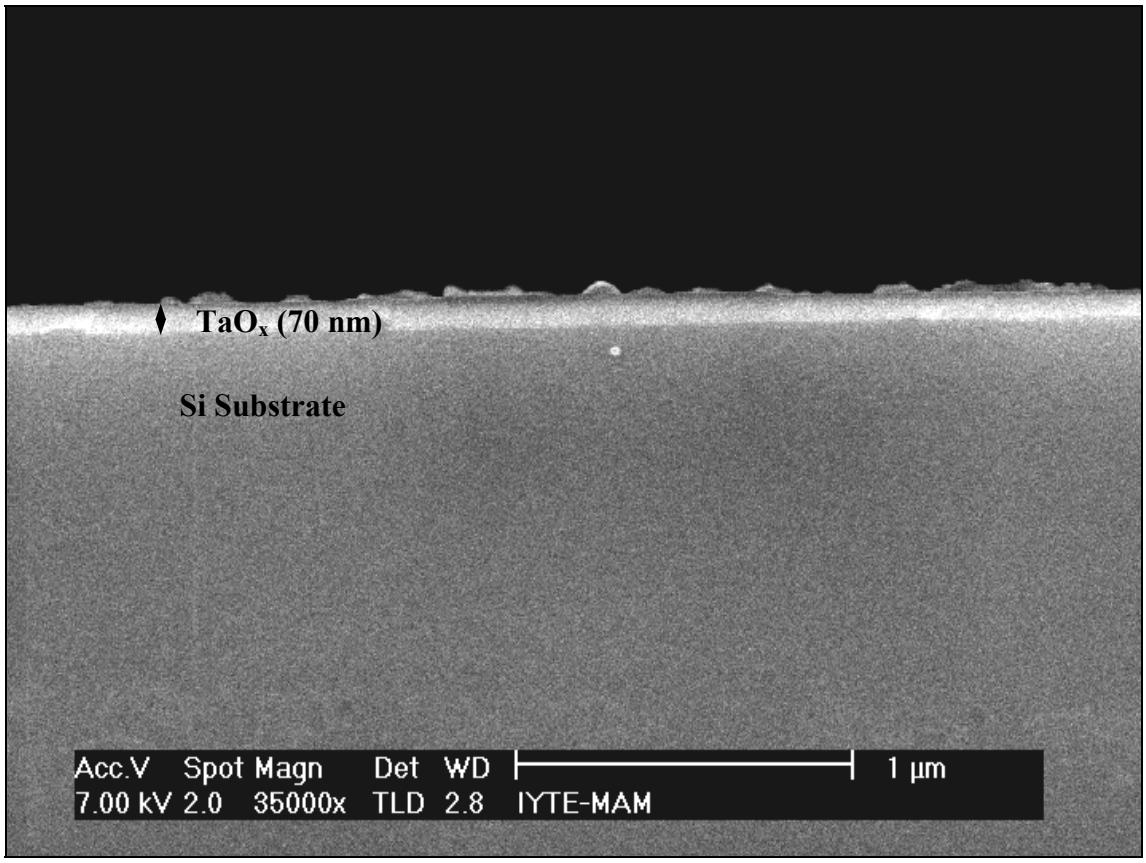

Figure 4.18. SEM cross-section micrograph of TaO_x (70 nm) on Si (001).

Fig. 4.18 illustrates the cross-section view of TaO_x on Si (001) sample. From this figure, TaO_x exhibits uniform deposition but surface of the sample seems to be quite rough containing some kind of big structures on the surface. This is in good agreement with the AFM roughness measurements also. In AFM, average roughness for TaO_x surface was found to be 1.1 nm which is quite rough for thin film applications. In addition, thickness was confirmed with the value of 70 nm.

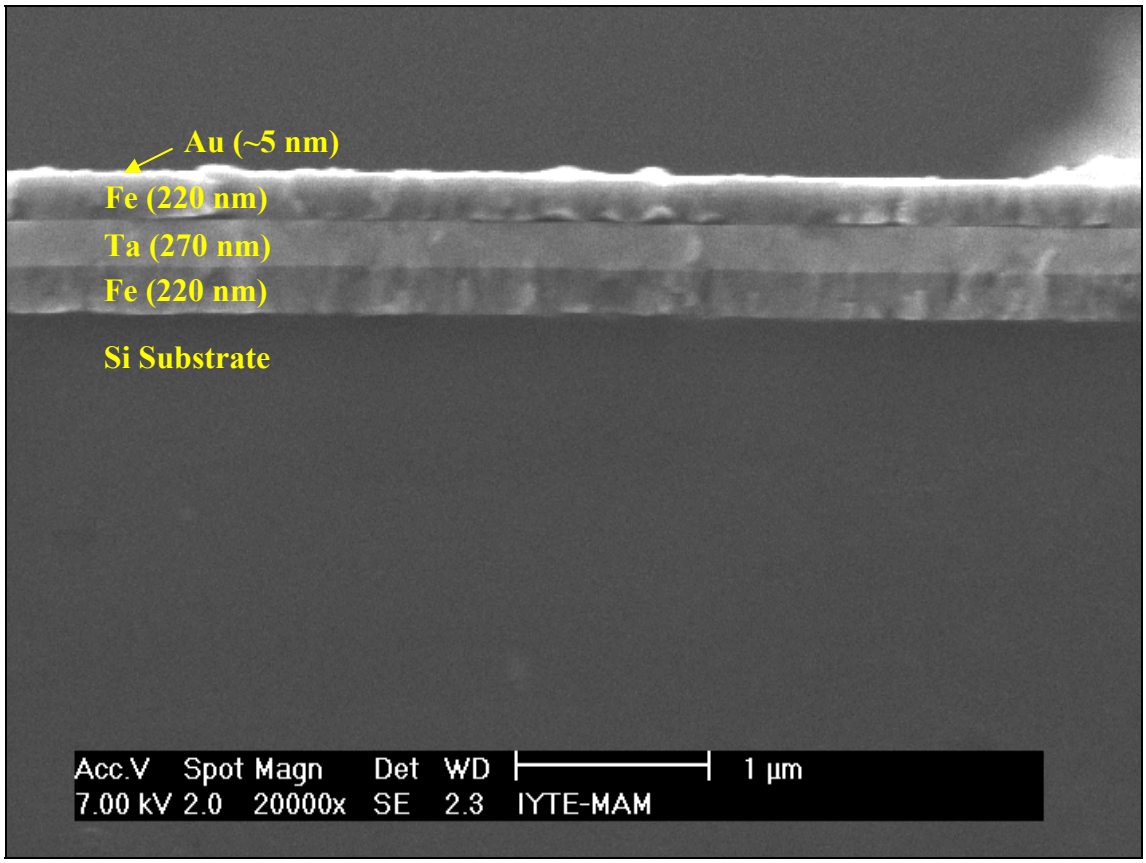

Figure 4.19. SEM cross-section micrograph of Si/Fe (220nm)/Ta (270nm)/Fe (220nm)/Au (~5nm).

Completing the SEM cross-section analysis of single layers, as-grown multilayers were investigated and their micrographs are shown in Fig. 4.19 - 4.22. In Fig. 4.19, thick Si/Fe/Ta/Fe/Au multilayer is illustrated. Layers of Fe and Ta can be clearly observed with capping layer of gold. Thicknesses of the layers were found to be 220 nm and 270 nm for iron and tantalum layers, respectively. Uniform depositions of both iron and tantalum layers are obvious in the micrograph. Furthermore, there is no evidence of intermixing at the interfaces at 20000x magnification.

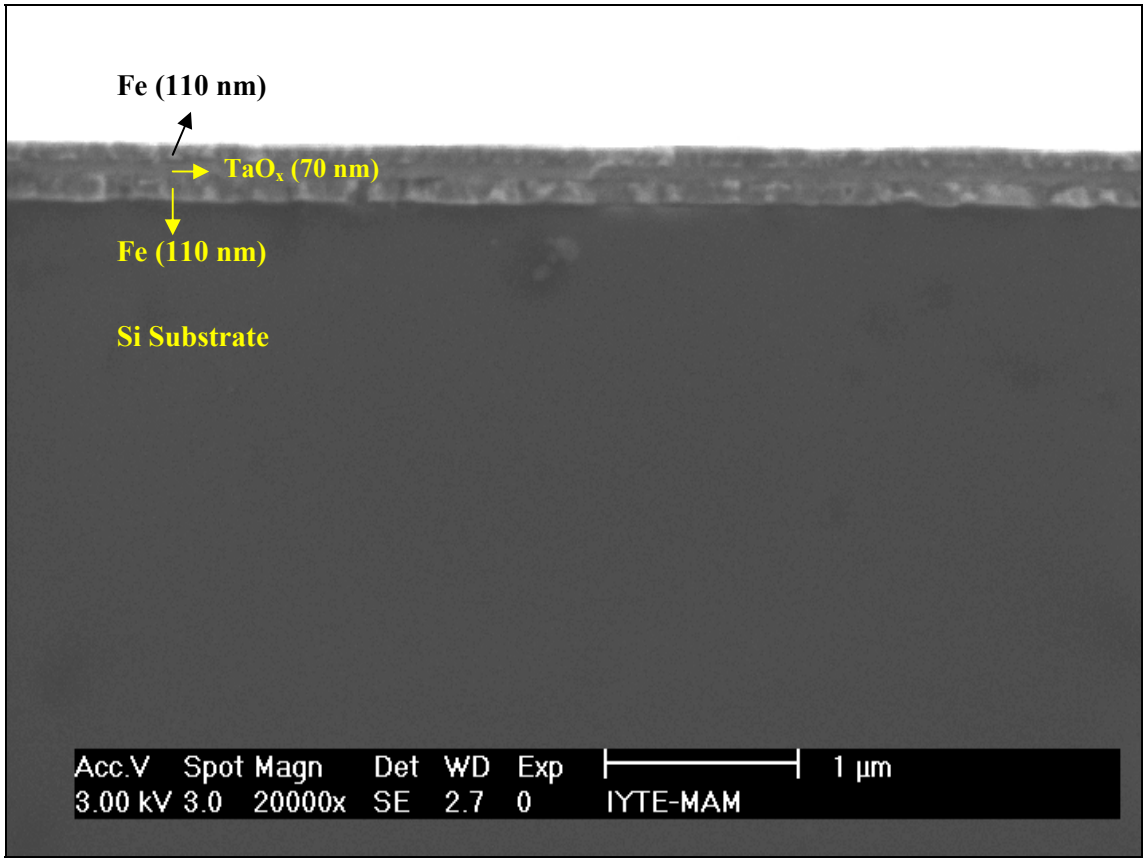

Figure 4.20. SEM cross-section micrograph of Si/Fe(110nm)/TaO_x(70nm)/Fe(110nm).

Fig. 4.20 shows cross-section image of Si/Fe(110nm)/TaO_x(70nm)/Fe(110nm) sample. Each layer of iron and tantalum oxide is clear in the micrograph. Films seem to be very uniform and there is no evidence of intermixing at this magnification. Thicknesses of the layers were found to be as expected. One thing to notice is the difference between the top and the bottom iron layers. Top iron layer seems in different orientation (Si(100)/Fe(110)//Ta(110)//Fe(200)) then the bottom one. This may be the reason for the second peak formation that was found in XRD analysis.

EDX analysis on Si substrate, single layer, and multilayers are summarized in Table 4.3. The weight percent of iron, tantalum, oxygen, gold and silicon is shown in the table. The oxygen content in the substrate and the other samples are investigated to understand the oxidation amount in the samples. Si substrate contains less than 2 % oxygen. This amount will be subtracted while interpreting the oxygen amount in the samples.

Fe single layer seems to contain 1% oxygen this amount is very low and negligible in our study. In addition, EDX measurement is not so reliable values below 5%. That means sample might have smaller amount of oxygen. Oxygen amount in tantalum single layer is quite low when substrate effect is subtracted because EDX gives 0.59% oxygen content.

TaO_x single layer contains 12% oxygen and 88% tantalum when the ratios of the EDX percents are considered. This oxygen amount is quite low compared to Ta_2O_5 which has 18.1% of oxygen (WEB_1) in it. That means reactive oxidation of tantalum does not result in exact tantalum pentoxide phase in our sputtering system according to EDX. On the other hand, for the thick $Fe/TaO_x/Fe$ multilayer, oxygen content of TaO_x layer seem to decrease whereas thin multilayer sample has higher oxygen amount which is 20 %. This might be a result of growth process of tantalum oxide. Bottom iron layer could be more oxidized in this sample because there is oxygen in the chamber during growth. At the beginning of growth of TaO_x layer, it might take some time to start growing. This situation may result in oxidation of iron layer and EDX might give high oxygen content for this sample.

Table 4.3. EDX weight percent results for all samples.

Sample	**Iron (Wt %)**	**Tantalum (Wt %)**	**Oxygen (Wt %)**	**Gold (Wt %)**	**Silicon (Wt %)**
Si (001) Substrate	0	0	1.38	0	98.62
Si/Fe (220nm)	82.56	0	3.62	0	13.82
Si/Ta (270nm)/Au	0	92.25	0.59	3.72	3.45
Si/TaO_x(70nm)	0	84.05	11.24	0	4.71
Si/Fe(220nm)/Ta(270nm)/Fe(220nm)/Au	43.99	49.41	2.47	3.46	0.68
Si/Fe(50nm)/Ta(30nm)/Fe(50nm)/Au	49.19	34.39	2.09	14.00	0.29
$Si/Fe(110nm)/TaO_x$(70nm)/Fe(110nm)	58.12	29.50	4.24	0	7.14
$Si/Fe(50nm)/TaO_x$(35nm)/Fe(50nm)/Au	56.61	18.87	5.26	13.28	5.98

However, EDX measurement is not very reliable for values below 5%. Therefore, the ellipsometry technique is used to analyze the chemical composition of tantalum oxide film. In this experiment, refractive index of the tantalum oxide film on Si substrate was found as 2.1 (at 633 nm) as shown in Fig. 4.21. In literature, refractive index of Ta_2O_5 was reported in between 2.1-2.4 depending on the deposition conditions.

Therefore, we can conclude that our reactive oxidation of tantalum probably results in amorphous Ta_2O_5 film.

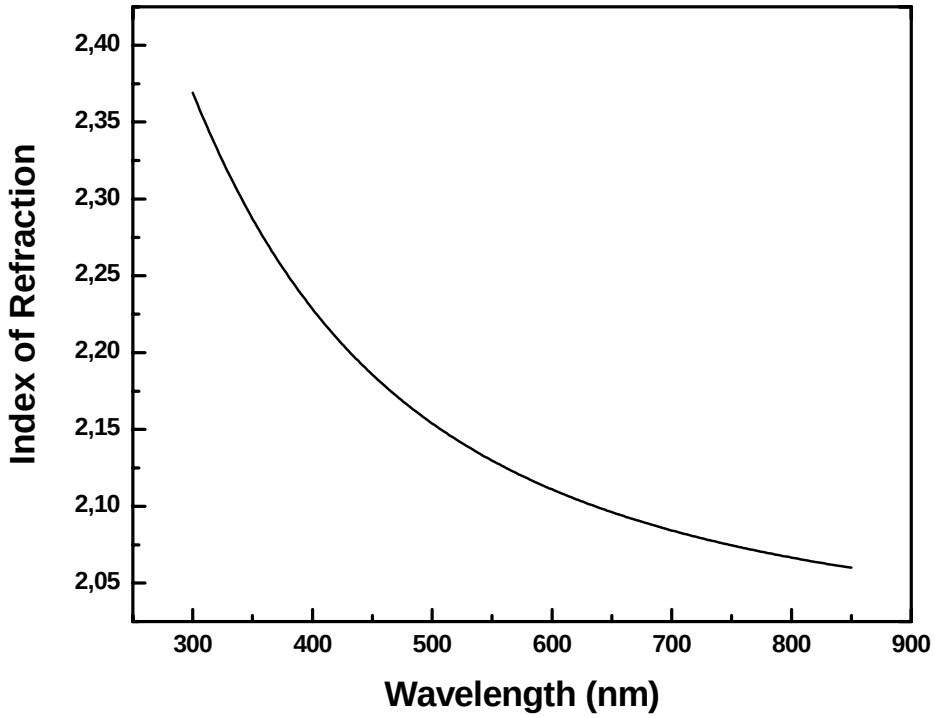

Figure 4.21. Ellipsometry measurement for TaO_x single layer.

In addition to refractive index, ellipsometry gives thickness of the layer and it was found to be 86.9 nm for tantalum oxide film. Furthermore, ellipsometry measurement yielded that there is 1.6 nm SiO_2 layer on the Si substrate as illustrated in Fig. 4.22. This SiO_2 layer may probably be a combination of native oxide on Si substrate and the oxide layer formed during deposition of tantalum oxide.

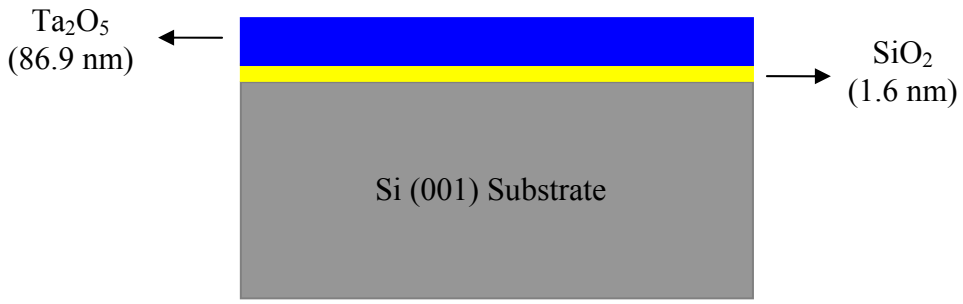

Figure 4.22. Schematic illustration of ellipsometry result of TaO_x on Si (001).

4.4. SQUID Magnetometer Results

Fig. 4.23 illustrates the hysteresis loop taken for 50 nm thick Fe single layer film on Si (001) substrate. It is easily observed that iron film is ferromagnetic with ~20 Oe coercive field and ~$1.6x10^3$ kA/m saturation magnetization. The saturation field is 30 Oe. These values are very close to bulk values of iron.

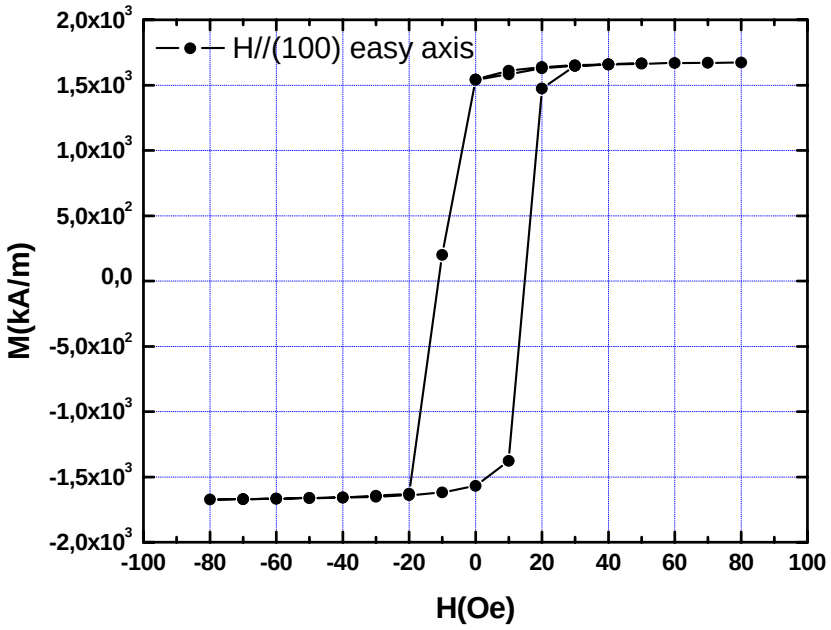

Figure 4.23. Hysteresis loop of Au (~5 nm)/Fe (50 nm)/Si (001).

CHAPTER 5

CONCLUSIONS

Fe/TaO_x/Fe magnetic multilayers were grown by magnetron sputtering method and structural characterization of these layers was performed by AFM, XRD and SEM techniques. AFM measurements of the samples yielded that iron and tantalum single layers were quite smooth and uniform but tantalum oxide was very rough compared to iron and tantalum films. AFM thickness measurements showed that growth rate was 0.3 Å/s for iron, 0.5 Å/s for tantalum and 0.2 Å/s for tantalum oxide. In addition, bilayers showed that tantalum on iron has rougher surface than single layer on Si and TaO_x on iron showed quite smooth surface compared to TaO_x on Si.

SEM measurements of all single layers, bilayers and multilayers showed that we have uniform continuous deposition of each layer. Thickness values were double-checked by using SEM cross-section micrographs. Multilayers with thinner layers were not easily investigated by SEM because resolution of our device was 20-30 nm. These multilayers have ~30 nm thick layers of iron, tantalum or tantalum oxide layers. EDX analysis yielded that we have very small oxygen content in iron, tantalum, and silicon. On the other hand, EDX analysis of TaO_x layer showed that it is not in the form of tantalum pentoxide which is the most stable oxide of tantalum. Our tantalum oxidation resulted in less oxygen content than tantalum pentoxide according to EDX results. On the contrary, ellipsometry measurement indicated that tantalum oxide layer had the similar properties with Ta_2O_5 with a refractive index of 2.1 which is the same with tantalum pentoxide. Therefore, we can conclude that reactive oxidation of tantalum in our system results in Ta_2O_5 film.

XRD analysis of single layer growth of iron, tantalum and tantalum oxide samples showed that; Fe grew 45^0 tilted epitaxial single crystal on Si with ~0.5 degree FWHM and ~18 nm grain size due to low lattice mismatch between iron and silicon, tantalum single layer was not as good as iron layer with 3.89 degree FWHM and ~2 nm grain size. Namely, XRD pattern proved it to be low crystal quality with wide and low intensity (110) peak of tantalum. This is mainly a result of large lattice mismatch between tantalum and silicon. On the other hand, reactive sputtering of tantalum metal

resulted in amorphous tantalum pentoxide film on Si (001). Actually, these single layer growth results are in good agreement with the literature.

The bilayers of Si(001)/Fe/Ta, Si(001)/Ta/Fe, Si(001)/Fe/TaO_x, and Si(001)/TaO_x/Fe were deposited to understand the degree of crystallinity of each layer on top of another. From XRD measurements of these samples, tantalum showed good crystal structure on Fe with 0.72 degree FWHM and 14 nm grain size and it is single crystal because only one diffraction peak was observed in the XRD spectrum. But iron did not showed good crystallization on tantalum which is a basic result of physics of growth. This iron layer has the second peak formation which is (200). Furthermore, there is a sharp decrease in the intensity of (110) peak. This may be explained in a way that Fe grows in (200) orientation on Ta. On the other hand, Fe grows well on TaO_x with (110) diffraction peak formation. TaO_x grew in amorphous phase on Fe also.

XRD patterns of multilayers with different thicknesses showed similar behaviors with single and bilayers. There was a difference in intensities of peaks in thin multilayer structures. This is directly because of the thickness difference. Moreover, gold (111) peak was clearly observed in these multilayers due to the gold capping.

Hysteresis loop taken by squid magnetometer at room temperature showed that Fe film of thickness of 50 nm is ferromagnet and the magnetization value is comparable with that of the bulk Fe value.

REFERENCES

Androulakis, J., Gardelis, S., Giapintzakis, J., Gagaodakis, E. and Kiriakidis, G. 2005. ”Indium Oxide as a Possible Tunnel Barrier in Spintronic Devices”, *Thin Solid Films.* Vol. 471. p. 293.

Baibich, M.N., Broto, J.M., Fert, A., Nyugen Van Dau, F., Petroff, F., Eitenne, P. Creuzet, G., Friederich, A., and Chazelas, J. 1988. “Giant Magnetoresistance of (001)Fe/(001)Cr Magnetic Superlattices”, *Physical Review Letters.* Vol. 61, No. 21, p. 2472.

Barthélémy, A., Fert, A., Contour, J-P., Bowen, M., Cros, V., De Teresa, J.M., Hamzic, A., Faini, J.C., George, J.M., Grollier, J., Montaigne, F., Pailloux, F., Petroff, F. and Vouille, C. 2002. “Magnetoresistance and Spin Electronics”, *Journal of Magnetism and Magnetic Materials.* Vol. 242-245, p. 68.

Bauer, E. Z. 1958. *Kristallography.* Vol. 10, p. 423.

Berg, S. and Nyberg, T. 2005. “Fundamental Understanding and Modeling of Reactive Sputtering Processes”, *Thin Solid Films.* Vol. 476, No. 2, pp. 215-230.

Boubeta , C.M., Cebollada, A., Calleja, J.F., Contreras, C., Peiro, F., and Cornet, A. 2003. “Magnetization Reversal and Magnetic Anisotropies in Epitaxial Fe/MgO and Fe/MgO/Fe Heterostructures Grown on Si (001)”, *Journal of Applied Physics.* Vol. 93, No. 4, p. 2126.

Bowen, M., Cros, V., Petroff, F., Fert, A., Boubeta, C.M., Costa-Krämer, J.L., Anguita, J.V., Cebollada, A., Briones, F., De Teresa, J.M., Morellón, L., Ibarra, M.R., Güell, Peiró, F. and Cornet, A. 2001. “Large Magnetoresistance in Fe/MgO/FeCo(001) Epitaxial Tunnel Junctions on GaAs(001)”, *Applied Physics Letters.* Vol. 79, No. 11, p. 1655.

Brinkman, W.F., Dynes, R.C. and Rowell, J.M. 1970. “Tunneling Conductance of Asymmetrical Barriers”, *Journal of Applied Physics.* Vol. 41, No. 5, p. 1879.

Chaneliere, C., Four, S., Autran, J.L., and Devine, R.A.B., 1999. “Comparison between the Properties of Amorphous and Crystalline Ta_2O_5 Thin Films Deposited on Si”, *Microelectronics Reliability.* Vol. 39, p. 261.

Chapman, B., 1980. *Glow Discharge Processes*, (Wiley, New York), pp. 49-76.

Costa-Krämer, J.L, Anguita, J., Martin, J.I., Boubeta, C.M., Cebollada, A. and Briones, F., 2002. “Magnetic Coupling in Epitaxial Fe/MgO/Fe Microtunnel Junction Arrays”, *Nanotechnology.* Vol. 13, p. 695.

Cullity, B.D. and Stock, S.R. 2001. *Elements of X-Ray Diffraction*, (Prentice Hall, New Jersey), pp. 103-184.

Demiryont, H., Sites. J.R. and Geib, K. 1985."Effects of Oxygen Content on the Optical Properties of Tantalum Oxide Films Deposited by Ion-Beam Sputtering", *Applied Optics.* Vol. 24, No. 4, p. 490.

Dimitrova, T., Arshak, K., and Atanassova, E. 2001. "Crystallization Effects in Oxygen Annealed Ta_2O_5 Thin Films on Si", *Thin Solid Films*. Vol. 381, p. 31.

Dimopoulos, T., Gieres, G., Colis, S., Wecker, J., Luo, Y. and Samwer, K. 2003. "Magnetic Tunnel Junctions with Yttrium Oxide Barrier", *Applied Physics Letters.* Vol. 83, No. 16, p. 3338.

Dinia, A., Carrof, P., Schmerber, G. and Ulhacq, C. 2003. "Indirect Exchange Coupling Between Two Ferromagnetic Electrodes through ZnS Barrier in Magnetic Tunnel Junctions", *Applied Physics Letters.* Vol. 83, No. 11, p. 2202.

Dorneles, L.S., Sommer, R.L. and Schelp, L.F. 2002. "Tunnel Magnetoresistance in NiFe/TaO_x/Al_2O_3/Co Junctions with a Thin TaO_x Layer", *Journal of Applied Physics.* Vol. 91, No. 10, p. 7971.

Duke, C. B. 1969. *Tunneling in Solids,* (Academic Press, New York).

Ezhilvalavan, S. and Tseng, T.-Y. 2000. "Electrical Properties of Ta_2O_5 Thin Films Deposited on Cu", *Thin Solid Films.* Vol. 360, p. 268.

Gillies, M.F., Kuiper, A.E.T., Van Zon, J.B.A. and Sturm, J.M. 2001. "Magnetic Tunnel Junctions with Tantalum Oxide Barriers Displaying a Magnetoresistance Ratio up to 10% at Room Temperature", *Applied Physics Letters.* Vol. 78, No. 22, p. 3496.

Gregg, J.F., Petej, I., Jouguelet, E., and Dennis, C. 2002. "Spin Electronics-a review", *Journal of Physics D: Applied Physics.* Vol. 35, pp. R121-R155.

Gustavsson, F., George, J-M., Etgens, V. H. and Eddrief, M. 2001. "Structural and Transport Properties of Epitaxial Fe/ZnSe/FeCo Magnetic Tunnel Junctions", *Physical Review B.* Vol. 64, p. 184422.

Julliere, M. 1975. "Tunneling Between Ferromagnetic Films", *Physics Letters*, Vol. 54A, No. 3, p. 225-226.

Keavney, D.J., Fullerton, E.E. and Bader, S.D. 1997. "Perpendicular Conductance and Magnetic Coupling in Epitaxial Fe/MgO/Fe(100) Trilayers", *Journal of Applied Physics.* Vol.81, No. 2, p. 795.

Koller, P.H.P., De Jonge, W.J.M. and Coehoorn, R. 2005. "Barrier Thickness Dependence of the Magnetoresistance in TaO_x Magnetic Tunnel Junctions", *Journal of Applied Physics.* Vol. 97. p. 083913.

Ladak, S. and Hicken, R.J. 2005. "Evidence for Hot Electron Magnetocurrent in a Double Barrier Tunnel Junction Device", *Applied Physics Letters.* Vol. 87, p. 232504.

LeClair, P. Moodera, J.S., and Meservey R. 1994. “Ferromagnetic-Ferromagnetic Tunneling and The Spin Filter effect”, *Journal of Applied Physics.* Vol. 76, No. 10, p. 6546.

Li, Z., De Groot, C. and Moodera, J.H. 2000. “Gallium Oxide As an Insulating Barrier for Spin-dependent Tunneling Junctions”, *Applied Physics Letters.* Vol. 77, No. 22, p.3630.

Maekawa, S. and Gäfvert, U. 1982. “Electron Tunneling Between Ferromagnetic Films”, *IEEE Transactions on Magnetics.* Vol. 18, No. 2, p. 707.

McGuire, T.R. and Potter, R.I. 1975. “Anisotropic Magnetoresistance in Ferromagnetic 3d Alloys” *IEEE Transactions on Magnetics*. Vol. 11, No. 4, p. 1018.

Mitani, S., Moriyama, T. and Takanashi, K. 2003. “Fe/MgO/FeCo(100) Epitaxial Magnetic Tunnel Junctions Prepared by Using *in situ* Plasma Oxidation”, *Journal of Applied Physics.* Vol. 93, No. 10, p. 8041.

Mitsuzuka, T., Matsuda, K., Kamijo, A., and Tsuge, H. 1999. ”Interface Structures and Magnetoresistance in Magnetic Tunnel Junctions”, *Journal of Applied Physics.* Vol. 85, No. 8, p. 5807.

Miyazaki, T., Yaoi, T. and Ishio, S. 1991. “Large Magnetoresistance Effect in 82Ni-Fe/Al-Al_2O_3/Co Magnetic Tunneling Junction”, *Journal of Magnetism and Magnetic Materials.* Vol. 98, No. 1-2, p. L7-L9

Miyazaki, T. and Tezuka, N. 1995. “Giant Magnetic Tunneling Effect in Fe/Al_2O_3/Fe Junction”, *Journal of Magnetism and Magnetic Materials.* Vol. 139, No. 3, p. L231.

Moodera, J.S., Kinder, L.R., Wong, T.M. and Meservey, R. 1995. “Large Magnetoresistance at Room Temperature in Ferromagnetic Thin Film Tunnel Junctions”, *Physical Review Letters.* Vol. 74, No. 16, p. 3273.

Nabarro, F. R. N., 1983. *Dislocations in Solids* (North Holland, Amsterdam), Vol 6, p. 124.

Neidhart, J., Hultman, L., Abendroth, B., Gago, R. and Möller, W. 2003. “Diagnostics of a N_2/Ar Direct Current Magnetron Discharge for Reactive Sputter Deposition of Fullerene-like Carbon Nitride Thin Films”, *Journal of Applied Physics*. Vol. 94, No. 11, p. 7059-7066.

Nishimura, Y., Shinkawa, A., Ujita, H., Tsuji, M., and Nakamura, M. 1998. ”Deposition of Tantalum Oxide Films by ArF Excimer Laser Ablation”, *Applied Surface Science.* Vol. 136, p. 22.

Nowak, J. and Rauluszkiewicz, J. 1992. “Spin Dependent Electron Tunneling Between Ferromagnetic Films”, *Journal of Magnetism and Magnetic Materials.* Vol. 109, No. 1, p. 79.

O'Handley R. C., 1999. *Modern Magnetic Materials: Principles and Applications.* (John Wiley & Sons, New York)

Ohring, M., 2002. *Material Science of Thin Films.* (Academic Press, San Diego)

Park, B.G., Lee, T.D., Lee, T.H., Kim, C.G. and Kim, C.O. 2003. "Magnetic Tunnel Junctions With Hf Oxide and Modified Hf Oxide Tunnel Barriers". *Journal of Applied Physics.* Vol. 93, No. 10, p. 6423.

Platt, C.L., Dieny, B. and Berkowitz, A.E. 1997. "Spin Polarized Tunneling in Reactively Sputtered Tunnel Junctions", *Journal of Applied Physics.* Vol. 81, No. 8, p. 5523.

Przybylski, M., Grabowski, J., Zavaliche F., Wulfhekel, W., Scholz, R. and Kirschner, J. 2002. "Structural and Magnetic Characterization of Single-crytalline Fe/MgO/Fe Magneto-tunnel Junctions Grown on GaAs(001) and InP(001)", *Journal of Physics D: Applied Physics.* Vol. 35, p. 1821.

Riekkinen, T. and Molarius, J. 2003. "Reactively Sputtered Tantalum Pentoxide Thin Films for Integrated Capacitors", *Microelectronic Engineering.* Vol. 70, p. 392.

Rottländer, P., Hehn, M., Lenoble, O. and Schuhl, A. 2001. "Tantalum Oxide as an Alternative Low Height Tunnel Barrier in Magnetic Junctions", *Applied Physics Letters.* Vol. 78, No. 21, p. 3274.

Samarth, N., Chun, S.H., Ku, C.H., Potashnik, S.J. and Schiffer, P. 2003. "Hybrid Ferromagnetic/Semiconductor Heterostructures for Spintronics", *Solid State Communications.* Vol. 127, p. 173.

Sharma, M., Bae, S.-Y. and Wang, S.X. 2004. "Inelastic Electron Tunneling Spectroscopy of Magnetic Tunnel Junctions with AlN and AlON Barriers", *Journal of Magnetism and Magnetic Materials.* Vol. 272-276, p. 1952.

Shim, H.J., Hwang, I.J., Kim, K.S., Cho, B.K., Kim, J.-T. and Sok, J.H. 2002. "Voltage Dependence of Magnetoresistance in Magnetic Tunnel Junctions with AlN Tunnel Barrier", *Journal of Applied Physics.* Vol. 92, No. 2, p.1095.

Simmons, J.G. 1963. "Generalized Formula for the Electric Tunnel Effect between Similar Electrodes Separated by a Thin Insulating Film", *Journal of Applied Physics.* Vol. 34, No. 6, p. 1793.

Smits, C.J.P., Filip, A.T., Kohlhepp, J.T., Swagten, H.J.M., Koopmans, B. and De Jonge, W.J.M. 2004. "Magnetic and Structural Properties of EuS for Magnetic Tunnel Junction Barriers", *Journal of applied Physics.* Vol. 95, No. 11, p. 7405.

Takahashi, H., Soeya, S., Hayakawa, J., Ito, K., Kida, A., Asano, H. and Matsui, M. 2004. "Half-Metallic Fe_3O_4 Films for High-Sensitivity Magnetoresistive Devices", *IEEE Transactions on Magnetics.* Vol. 40, No.1, p. 313.

Tsang, C., Fontana, R.E., Tsann L., Heim, D.E., Speriosu, V.S., Gurney, B.A., and Williams, M.L. 1994. ”Design, Fabrication and Testing of Spin-Valve Read Heads for High Density Recording”, *IEEE Transactions on Magnetics*. Vol. 30, p. 3801.

Wang, D., Nordman, C., Daughton, J.M., Qian, Z., and Fink, J. 2004. “70% TMR at Room Temperature for SDT Sandwich with CoFeB as Free and Reference Layers”, *IEEE Transactions on Magnetics.* Vol. 40, No. 4, p. 2269.

Wang, J., Freitas, P.P., Snoeck, E., Wei, P. and Soares, J.C. 2001. “Spin-dependent Tunnel Junctions with ZrO_x Barriers”, *Applied Physics Letters.* Vol. 79, No. 26, p. 4387.

Wang, X. and Taratorin A.M., 1999. *Magnetic Information Storage Technology*. (Academic Press, NewYork,).

WEB_1, 2006. Webelements Periodic Table, 10/April/2006. http://www.webelements.com.

Wolf, E. L., 1985. *Principles of Electron Tunneling Spectroscopy.* (Oxford University Press, London).

Yaegashi, S., Kurihara, T., Sato, K., and Segawa, H. 1994. ”Epitaxial Growth and Magnetic Properties of Fe Films on Si Substrates”, *IEEE Transactions on Magnetics.* Vol. 30, No. 6, p. 4836.